

DTIC FILE COPY

(2)

AD-A222 537

IC  
STE  
4 1990

D

TECHNICAL REPORT CTI-TR-9005 ✓

A SOLID-STATE MULTIPLE-PASS  
AMPLIFIER FOR DIODE PUMPED  
COHERENT LASER RADAR SYSTEMS

APRIL 1990

CONTRACT NUMBER N00014-89-C-0220

Prepared for

Erhard Schimitschek  
Code 84  
Naval Ocean Systems Center  
271 Catalina Blvd.  
San Diego, CA 92152-5000  
(619) 553-3727

By

Sammy W. Henderson  
Charley P. Hale

Coherent Technologies, Inc.  
P.O. Box 7488  
Boulder, CO 80306  
(303) 449-8736

**DISTRIBUTION STATEMENT A**

Approved for public release  
Distribution Unlimited

90 05 29 079

## FOREWORD

This technical report presents the results of work performed by Coherent Technologies, Inc., Boulder, Colorado for a Phase I SBIR through the SDIO/IST under contract number N00014-89-C-0220. The period of performance was 1 September 1989 to 28 February 1990. The technical monitor for this contract was Erhard Schimitschek at the Naval Ocean Systems Center, San Diego, CA.

## ACKNOWLEDGMENTS

The authors are grateful to a number of people who directly contributed to this technical effort: Stuart Beaton of the University of Colorado, and James R. Magee at Coherent Technologies, Inc.; and valuable technical discussions with Murray Reed at Stanford University, Sol F. Laufer at ZYGO Corporation, and Chuck Grasse at Spectra Diode Laboratories. Much of the equipment used in the laboratory evaluations during this effort was assigned to contract number F33615-88-C-1756 monitored by Lt. Scott H. McCracken at Wright Patterson AFB. We are grateful to WPAFB for allowing us to use this equipment.



STATEMENT "A" per Erhard Schimitschek  
Naval Ocean Systems Center/Code 84  
271 Catolina Blvd., San Diego, CA 92152-5000  
TELECON 5/30/90 VG

Accession For	
NTIS CRA&I	<input checked="checked" type="checkbox"/>
DTIC TAB	<input type="checkbox"/>
Unannounced	<input type="checkbox"/>
Justification	
By <i>per call</i>	
Distribution/	
Availability Codes	
Dist	Avail and/or Special
A-1	

# TABLE OF CONTENTS

	<u>Page No.</u>
1. Introduction . . . . .	1
2. Background . . . . .	3
3. Theory . . . . .	5
3.1 Single-Pass Amplification . . . . .	6
3.2 Multiple-Pass Amplification of Long Pulses . . . . .	9
Output Energy . . . . .	13
Extraction Efficiency . . . . .	15
Output Power . . . . .	19
Pulse Shape Distortion . . . . .	20
4. High Performance Zig-Zag Slab Issues . . . . .	23
4.1 Recommended Slab Fabrication Procedure and Estimated Cost . . . . .	30
5. Results of Experimental Evaluation . . . . .	32
5.1 Description of Multiple-Pass Amplifier System . . . . .	32
5.2 Multiple-Pass Operation and Gain Characterization . . . . .	35
Small-Signal Gain . . . . .	35
Multiple-Pass Pulse Energy Characterization . . . . .	37
5.3 Spatial Beam Quality Evaluations . . . . .	46
Passive CW Operation . . . . .	49
Single-Shot Operation . . . . .	50
High Average Power Operation . . . . .	53
6. Preliminary Design of a Diode-Pumped High Performance Slab Amplifier . . . . .	56
6.1 Pump Source Considerations . . . . .	56
6.2 Preliminary Design of Diode-Pumped Amplifier . . . . .	57
Amplifier Pump Analysis . . . . .	57
Amplifier Geometry . . . . .	59
Cost Estimate . . . . .	63
7.0 Summary and Conclusions . . . . .	63
8.0 References . . . . .	65

## 1. Introduction

Requirements for a sensitive, accurate sensor for applications in space-based strategic defense and target recognition point to the need for the development of very robust, agile coherent laser radar instruments. Recent advances in high power pulsed and continuous-wave (CW) laser diode and diode array technology has prompted a renaissance in the use of solid-state laser transmitters in coherent and incoherent laser radar systems. In particular, all-diode-pumped coherent laser radar systems now appear feasible for ground-, air-, and space-based applications where electrical power (efficiency), size, and weight considerations are very important. The unattended lifetime, pulse repetition frequency (PRF), and beam quality of such an all-solid-state laser radar are expected to be improved upon over both CO<sub>2</sub> and flashlamp-pumped solid-state systems. In most applications where atmospheric turbulence is not too severe, the performance of the shorter wavelength all-solid-state laser radar systems exceeds that of the longer wavelength CO<sub>2</sub> systems.

The particular instrumental capabilities required in strategic defense applications strongly point to the development of a diode-pumped coherent laser radar configured as a compact Master Oscillator, Power Amplifier (MOPA) system. When compared to the alternative configuration, a long pulse, injection-seeded power oscillator, the MOPA offers distinct advantages. The MOPA configuration is ideally suited to introduce phase and amplitude modulation onto the transmitted pulse in order to produce fast, highly agile frequency tuning, chirping, and pulse amplitude shaping. Amplitude modulation allows variable pulse widths and pulse shapes to be transmitted, and combined phase and amplitude modulation allows high accuracy measurements of target range and velocity. In the system envisioned, this modulation is introduced on a low power CW beam from the highly stable master oscillator before injection into the amplifier system. Since the laser power at the modulator is low, low voltage integrated phase and amplitude modulators using Optical Guided Wave (OGW) technology could be utilized in place of large, high voltage

electro-optic (EO) modulators.

A disadvantage of the MOPA configuration is the inefficiency of the first few amplification stages due to lack of gain saturation. During this effort we addressed the development of a high-gain Nd:YAG preamplifier which minimizes the efficiency problem, allowing a single amplification stage to efficiently boost the power level from the low power MO, so that saturation fluences can be achieved in subsequent stages of amplification. The preamplifier we investigated utilizes a slab geometry which permits several angularly-multiplexed passes. As we show in this report, multiple passes through the preamplifier allows efficient use of the stored energy and hardware. In addition, the slab geometry reduces the thermal problems encountered under high PRF (high average power) operation.

A key difficulty of the multiple-pass slab design is the necessity of demanding flatness of the reflecting surfaces. The large number of bounces from the slab faces can lead to high accumulated wavefront distortion. The discussion of Section 4 and the experimental results of Section 5 show that high quality slabs of the proper dimensions for this application can be fabricated and that low distortion amplification can be achieved.

During this effort we utilized an existing flashlamp-pumped Nd:YAG slab to experimentally demonstrate that efficient preamplification of low energy pulses can be achieved. Using this less-than-ideal slab in a 4-pass amplifier configuration we demonstrated: 1) small signal gains exceeding 87 dB ( $> 5 \times 10^8$ ); 2) output pulse energies exceeding 50 mJ, for input pulse energies  $< 50$  nJ; and 3) spatial beam quality  $< 1.5$  times diffraction limited, even at moderately high average power.

In Section 6 we provide the preliminary design of a diode laser-pumped version of this slab preamplifier, which will be capable of amplifying low-energy amplitude modulated pulses from a low-power CW MO laser to energies of  $\geq 50$  mJ. This amplifier will operate at a PRF of 100 Hz and the spatial quality of the output pulses will be near diffraction limited.

## 2.0 Background

In this section we describe the geometry used in the high-gain Nd:YAG preamplifier. We also provide a summary of previous measurements made using this geometry.

Single-pass flashlamp-pumped gains of 20 dB can be achieved with Nd:YAG rods. At this level of gain, additional pump energy results primarily in increased amplified spontaneous emission (ASE). A chain of amplifiers potentially allows for a total gain equal to the product of all individual amplifier gains, if the rods are spatially separated to attenuate ASE. The use of multiple rods to achieve very high gain is inefficient if the input energy is so low that the gain is not saturated. Efficient use of energy and hardware would result if the gain medium were passed through repeatedly. However, a technique for overlapping several beams inside the gain volume while separating them externally is required. Polarization multiplexing is one possibility. A significant disadvantage of polarization multiplexing is the necessity for normal incidence optics to direct the beam back through the rod. Any surface at normal incidence may lead to parasitic oscillation of the amplifier.

Multiplexing can be achieved by utilizing the multiplicity of internal paths existing in an internally-reflecting zig-zag slab as shown in Figure 1. The slab geometry was developed to reduce thermally-induced optical distortion at high average power levels.<sup>1</sup> Usually the angles are chosen such that the direction of the beam outside the slab is along the long axis of the slab. This need not be the case. A typical slab permits a number of rays to enter the slab at the center of the entrance face, exit at the center of the exit face, and be totally internally reflected, as illustrated in Figure 1. Each such ray has a different number of total internal reflections and propagates at a different angle. Thus, beams centered about these rays separate outside the slab. This angular separation also allows the beam reinjection optics to remain at non-normal incidence, reducing the problem of parasitic oscillation and feedback into the oscillator source. Angular multiplexing in the slab laser

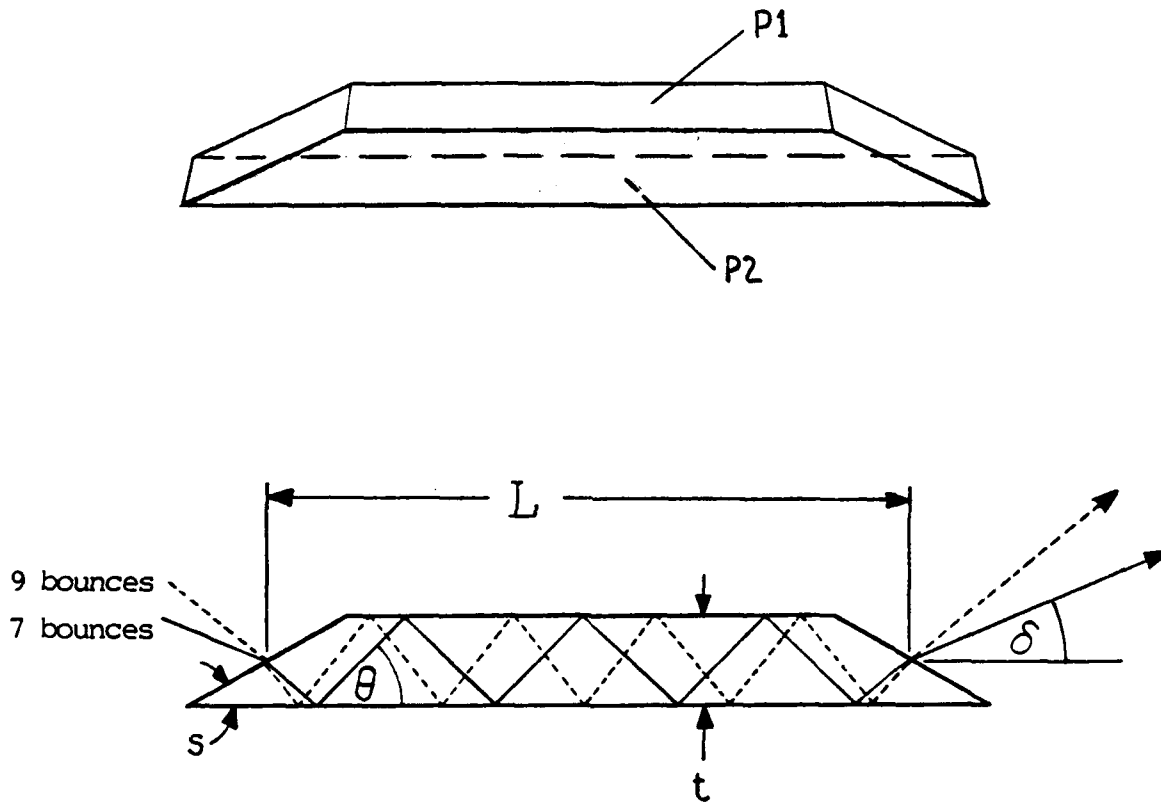


Figure 1. Geometry illustrating principle of angle-multiplexing in Nd:YAG slab preamplifier. Differing internal and external propagation angles produce multiple paths inside slab.

also allows the gain medium to be efficiently utilized.

The large number of total internal reflections of the slab faces can lead to high accumulated wavefront distortion unless the slab is fabricated properly. We discuss the fabrication issue in Section 4. The goal is efficient preamplification of a very low energy input pulse to a level sufficient to saturate following stages of amplification. The aspect ratio (width/thickness) of the Nd:YAG slabs we consider here is either 1 or 2. Although not usually used for slab laser applications, it has been demonstrated that unity aspect ratio slabs can perform well under reasonably high thermal loading.<sup>2,3</sup> While at Stanford University in 1985, Tom Kane demonstrated a flashlamp-pumped, multiple-pass, unity-aspect-ratio Nd:YAG slab amplifier having a 3-pass small-signal gain of 62 dB.<sup>4</sup> In 1987 we developed a similar amplifier for a 1.06  $\mu\text{m}$  coherent laser radar system.

Previous to the experimental work described in Section 5, we had used this amplifier in a 3-pass configuration to demonstrate small-signal gains of  $\sim 67$  dB.<sup>5</sup> For the laser radar application, this device was used to amplify 10 nJ input pulses, gated from the output of a single frequency CW MO, to an output energy of  $\sim 8$  mJ. Even though it is flashlamp pumped, the efficiency of this amplifier was  $\sim 3$  times greater than the one described in Ref. 4. The beam quality of the output was good up to the 13 Hz PRF possible with our existing flashlamp power supply. The goal of the current effort was to investigate techniques allowing even higher efficiency and high PRF operation from this type of device. The following sections summarize our efforts.

### 3.0 Theory

In this section we describe the amplification of long duration pulses in a high-gain multiple-pass amplifier. For most experimental configurations, highly accurate prediction of the amplifier behavior requires the numerical solution of coupled differential equations which describe the time evolution of the laser intensity and the population inversion density<sup>7,8</sup>. Rather



than perform the detailed numerical calculations here, we derive analytic expressions which approximate the temporal evolution of the gain, output power, and output energy. The analytic expressions are very useful for describing the general behavior, and for illustrating the important physics of these devices. In most cases, the performance predictions obtained using the approximate analytic solutions place a lower (i.e., conservative) bound on the true amplifier performance.

### 3.1 Single Pass Amplification

Figure 2 illustrates an input pulse making a single pass through a gain medium and being amplified. The thin temporal section at the leading edge of the input pulse, which exits the gain medium at  $t = 0$ , sees a total population inversion of  $N_0$  within its mode volume as it traverses the gain medium. Due to energy extraction from the gain medium by the preceding part of the input pulse, a thin temporal section of the pulse which exits the gain medium at a later time  $t$  sees a total population inversion of  $N(t) < N_0$  within its mode volume as it traverses the gain medium. Note that  $N(t)$  is not the population inversion at time  $t$ , defined as  $N_I(t)$ . In fact, due to energy extracted by succeeding parts of the pulse which are in the gain medium at time  $t$ ,  $N_I(t)$  is always less than  $N(t)$  during amplification.

If we assume that the reduction or increase in  $N$  due to spontaneous emission or pumping is negligible compared to that due to emission stimulated by the input pulse, we can write  $N(t)$  as

$$N(t) = N_0 - \Phi_{ex}(t), \quad (1)$$

where  $\Phi_{ex}(t)$  is the total number of photons extracted from the gain medium by the input pulse up until time  $t$ . Eq. (1) is simply obtained from conservation of particles (or conservation of energy).  $\Phi_{ex}(t)$  represents the photons making up the energy in the shaded region of Figure 2. Note that similar to  $N(t)$ ,  $\Phi_{ex}(t)$  is not the total number of photons which have been extracted from the inversion, defined as  $\Phi_{exI}(t)$ , since some

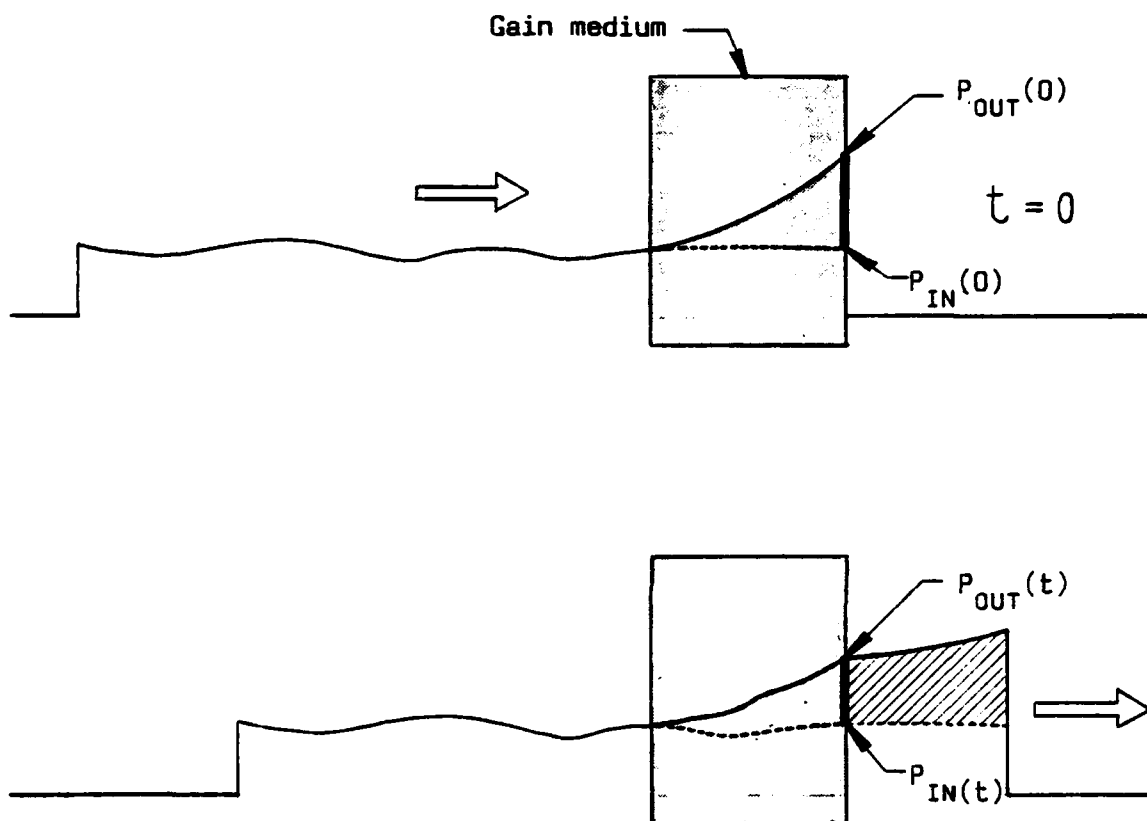


Figure 2. Illustration of the single-pass amplification process.

photons are still in the gain medium. The number of extracted photons is given by

$$\Phi_{ex}(t) = \frac{E_{ex}(t)}{h\nu} = \frac{1}{h\nu} \int_0^t [P_{out}(t') - P_{in}(t')] dt', \quad (2)$$

where  $E_{ex}$  is the extracted energy up until time  $t$ ,  $h$  is Planck's constant,  $\nu$  is the laser frequency, and  $P_{in}(t')$  and  $P_{out}(t')$  are the input and output powers at time  $t'$ , respectively. For Nd:YAG operating at  $1.06 \mu\text{m}$ , the fluorescence lifetime of the upper laser level is  $\sim 230 \mu\text{s}$ . Since we are primarily interested in amplifying pulses whose durations are  $0.5 \mu\text{s}$  to  $5.0 \mu\text{s}$ , the assumption used to obtain Eqs. (1) and (2) is very good as long as the pump rate during amplification is low. For the cases of interest here this is also true.

In order to easily obtain an analytic expression for the gain experienced by the input pulse vs time, we make two additional assumptions. First, we assume a plane-wave, top-hat transverse intensity profile of fixed diameter for the laser mode in the gain medium. Second, we assume that each cross sectional area within the laser mode sees the same number of inverted ions, irrespective of its transverse position. Note that this second assumption does not require the population inversion to be uniformly spread out over the entire laser mode. In other words, it does not require a uniform population inversion density, only that the integral of the population inversion density along the beam path be independent of transverse position in the beam. The analytic solutions that will be obtained using these assumptions contain most of the important physics of the problem and do not differ greatly from more detailed numerical solutions of typical laboratory cases where the transverse profiles of the input beam and inversion density are not uniform.

Under the assumptions described above, the gain experienced by the thin temporal section of the pulse which exits the gain medium at time  $t$  (see Figure 2), is simply given by Beer's law, which is

$$\frac{P_{out}(t)}{P_{in}(t)} = \exp \left[ \sigma \frac{N(t)}{V} L \right], \quad (3)$$

where  $\sigma$  is the stimulated emission cross section of the laser transition,  $V$  is the mode volume of the laser beam in the gain medium, and  $L$  is the length of the beam path in the gain medium. Note that  $L$  is not necessarily the length of the gain medium, defined as  $L_0$ , since the beam axis need not be parallel to the axis of the gain medium.

Substitution of Eqs. (1) and (2) into Eq. (3) gives

$$P_{out}(t) = P_{in}(t) G_0 \exp \left[ - \frac{\sigma L}{h\nu V} E_{ex}(t) \right], \quad (4)$$

where

$$G_0 = \exp \left[ \frac{\sigma L}{V} N_0 \right] = \exp \left[ \frac{\sigma L}{h\nu V} E_{stored} \right] \quad (5)$$

is the small signal (unsaturated) gain, with  $E_{stored}$  being the energy which is initially stored in the inversion which is inside the mode volume. Eq. (4) can be used to obtain analytic expressions for  $E_{out}$  and  $P_{out}$  as functions of the input energy vs time. These expressions are derived in the next subsection which describes multiple-pass amplification.

### 3.2 Multiple-Pass Amplification of Long Pulses

In a multiple-pass amplifier mirrors are used to direct the input beam through the amplifier gain medium a number of times. An expression for the gain vs time similar to that of Eq. (4), for the single pass case, is desired. Unfortunately, numerical solution of the coupled photon transport and rate equations is required in the general case which allows for any arbitrary input pulse, any number of passes, any degree of mode overlap between the mode volumes of individual passes, any time delay between individual passes, etc. (For a detailed description of amplifiers see Ref. 8.) The problem is greatly simplified if, in

addition to the assumptions which led to Eq. (4), we also assume that each pass through the amplifier encounters the same mode volume as all the previous passes did. Assuming that the mode volumes of individual passes through the gain medium are fixed, it can be shown that incomplete overlap of the mode volumes of separate passes will result in  $G(t)$ ,  $E_{out}(t)$  and  $P_{out}(t)$  being larger than those values calculated for the case where all mode volumes perfectly overlap. The assumptions allow analytic solutions to be obtained in the limit of pulses which are either short compared to the transit time between individual passes, or pulses which are very long compared to the transit time to complete all passes. In the short pulse limit, each of the passes can be considered independently and Eq. (4) can be used for each individual pass, with  $N_0$  for each pass being adjusted for the energy extracted in previous passes. Since our goal is to develop a high-gain Nd:YAG preamplifier for a coherent laser radar system, the primary interest here is in describing multiple-pass amplification of pulses such that the duration of the output pulses is between 0.5  $\mu s$  and 5.0  $\mu s$ . As we will show below, for the configurations under consideration, a modified version of Eq. (4) is a reasonably good approximation of the gain vs time obtained during the multiple-pass amplification of these long duration output pulses.

We consider the case where the input pulse is allowed to make  $n$  passes through the same mode volume. At any time  $t$ , the total inversion in the mode volume is given by  $N_I(t)$  and the total energy which has been extracted from the inversion is  $E_{exI}(t)$ . As described earlier, these two quantities differ from  $N(t)$  and  $E_{ex}(t)$ , which were used to derive Eq. (4).  $N_I(t)$  and  $E_{exI}(t)$  are coupled through the conservation of energy:

$$N_I(t) = N_0 - \frac{1}{h\nu} E_{exI}(t). \quad (6)$$

In cases where  $E_{exI}(t)$  and  $N_I(t)$  are slowly varying during the transit time for a single pass through the gain medium,  $L/c$ ,

$N_I(t)$  and  $N(t)$  are, for all practical purposes, the same. Thus, the gain experienced by a thin temporal section of light which traverses the gain medium at time  $t$  is given by

$$G(t) = P_{out}(t)/P_{in}(t) = \exp\left[\sigma \frac{N_I(t)}{V} L\right]. \quad (7)$$

This is identical to Eq. (3), except that  $N(t)$  has been replaced by  $N_I(t)$ . Eqs. (6) and (7) can be combined to obtain,

$$G(t) = G_0 \exp\left[-\frac{\sigma L}{h\nu V} E_{exI}(t)\right]. \quad (8)$$

For Eqs. (7) and (8) to be valid,  $E_{exI}(t)$  and  $N_I(t)$  must vary slowly enough that  $G(t) \sim G(t \pm L/c)$  for all times during the amplification process. For the cases of interest here (output pulse durations  $> 0.5 \mu s$  and  $L/c \lesssim 1 ns$ ), the approximation is excellent.

A thin temporal slice of the pulse which leaves the final  $n$ th pass through the amplifier at time  $t$  experiences an  $n$ th-pass gain of  $G(t)$ , given by Eq. (8). If the transit time between the  $m$ th pass and the final pass is given by  $t_m$ , the gain this same temporal slice experienced when it was making its  $m$ th pass is given by  $G(t-t_m)$ . Losses between individual passes through the gain medium reduce the output of the  $m$ th pass by a factor of  $A_m$  before it is reinjected into the gain medium for the  $(m+1)$ th pass. We also allow the input to the first pass to be reduced by  $A_0$  and the output of the  $n$ th pass to be reduced (attenuated) by  $A_n$ . Therefore, the total net multiple-pass gain experienced by the thin temporal slice of the pulse which leaves the final pass at time  $t$  is given by the product

$$G_T(t) = A_n G(t) \cdots A_m G(t-t_m) \cdots A_1 G(t-t_1) A_0. \quad (9)$$

By utilizing Eq. (8) and defining

$$G_{T_0} \equiv G_0^n, \quad \delta \equiv \frac{\sigma_L}{h\nu V}, \quad \text{and} \quad A_T \equiv \prod_{m=0}^n A_m \quad (10)$$

we can write Eq. (9) as

$$G_T(t) = A_T G_{T_0} \exp \left\{ -\delta \left[ E_{\text{exI}}(t-t_1) + \dots \right. \right. \\ \left. \left. + E_{\text{exI}}(t-t_m) + \dots + E_{\text{exI}}(t) \right] \right\}. \quad (11)$$

If we define

$$\Delta E_{\text{exI}}^m(t) \equiv E_{\text{exI}}(t) - E_{\text{exI}}(t-t_m), \quad (12)$$

Eq. (11) can be written as

$$G_T(t) = A_T G_{T_0} \exp \left[ -n\delta E_{\text{exI}}(t) \right] \exp \left[ \delta \sum_{m=1}^{n-1} \Delta E_{\text{exI}}^m(t) \right]. \quad (13)$$

In cases where  $E_{\text{exI}}(t)$  changes very little (varies slowly) over the multiple-pass transit time through the amplifier, the last exponential factor of Eq. (13) will be  $\sim 1$ , and Eq. (13) can be reduced to

$$P_{\text{out}}(t) = P_{\text{in}}(t) A_T G_{T_0} \exp \left[ -n\delta E_{\text{exI}}(t) \right]. \quad (14)$$

We refer to this as the long pulse limit of the more general Eq. (13). Assuming the same attenuation factor  $A_T$ , this result differs from that which would be obtained for a single amplifier whose small signal gain is  $G_{T_0}$ , or a linear chain of identical amplifiers whose combined small signal gain is  $G_{T_0}$ , only in that the last factor would be  $\exp[-\delta E_{\text{exI}}(t)]$  [see Eq. (4)]. Thus, the gain of a multiple-pass amplifier is saturated much more "quickly" than that of a single-pass amplifier, or a linear chain of amplifiers, having the same small signal gain.

If the stored energy is extracted so quickly that  $G_T(t)$

changes significantly over the multiple-pass transit time, the last factor in Eq. (13) will be significantly  $> 1$  and cannot be neglected if accurate solutions for  $E_{out}(t)$  and  $P_{out}(t)$  are desired. Even in these cases, the solutions of Eq. (14) place a lower bound on the true performance of the amplifier, underestimating  $G(t)$ ,  $E_{out}(t)$ , and  $P_{out}(t)$ . Since our primary goal is to describe the multiple-pass amplification of pulses where the stored energy is extracted (approximately uniformly) over time periods  $> 0.5 \mu s$ , and since multiple-pass transit times are of the order of 10 ns for practical configurations, the assumptions leading to Eq. (14) are not seriously violated for the cases of interest. With the above comments in mind, we proceed to obtain solutions of Eq. (14) for  $E_{out}(t)$  and  $P_{out}(t)$ .

#### Output Energy

For the cases we wish to describe, i.e., high-gain multiple-pass amplification of low energy, long duration pulses, almost all of the energy extraction occurs in the final pass. If we assume that throughout the amplification process any extracted energy which is present between the first and final pass, as well as any extracted energy which is lost due to attenuation (Fresnel reflections, absorption, etc.) before entering the final pass, is negligible, we obtain

$$E_{exI}(t) \sim \frac{1}{A_n} [E_{out}(t) - A_T E_{in}(t)]. \quad (15)$$

Once again, for all the cases we are considering, this is a good approximation. Using Eq. (15) and the relationship  $P(t) = dE(t)/dt$  in Eq. (14), yields

$$\frac{dE_{out}(t)}{dE_{in}(t)} = A_T G_{To} \exp \left\{ \frac{-n\delta}{A_n} [E_{out}(t) - A_T E_{in}(t)] \right\}. \quad (16)$$

By combining like terms, integrating, and solving for  $E_{out}(t)$  we obtain



$$E_{out}(t) = \frac{A_T}{\beta} \ln \left\{ 1 + G_{To} \left[ \exp(\beta E_{in}(t)) - 1 \right] \right\}, \quad (17)$$

where  $\beta = \frac{A_T}{A_n} n \delta = \frac{A_T}{A_n} \frac{n}{A} \frac{1}{F_{sat}}$  where  $F_{sat} = \frac{h\nu}{\sigma}$  is the saturation fluence and  $A$  is the cross sectional area of the mode volume  $V$ . This equation yields the expected results in the limit of both small and large  $E_{in}$ . If  $E_{in}$  is very large, so that  $e^{\beta E_{in}} \gg 1$ , we obtain

$$E_{out}(t) = A_n E_{stored} + A_T E_{in}. \quad (18)$$

The relation  $G_{To} = G_o^n$ , with  $G_o$  being defined in Eq. (5), was used to produce Eq. (18). This is the expected result since it represents full saturation and complete extraction of the energy stored in the mode volume. If  $E_{in}$  is very small, so that  $e^{\beta E_{in}} \sim 1 + \beta E_{in}$ , we obtain from Eq. (17)

$$E_{out}(t) = \frac{A_T}{\beta} \ln \left[ 1 + G_{To} \beta E_{in}(t) \right] \quad (19)$$

In the limit that  $E_{in}$  is also small enough that  $G_{To} \beta E_{in}(t) \ll 1$ , we obtain

$$E_{out}(t) = A_T G_{To} E_{in}(t), \quad (20)$$

which is the expected small signal gain result.

The gross energy gain of the amplifier, defined as the ratio of the energy of the amplified pulse to that of the unamplified but attenuated pulse at the same location, is given by

$$G_E = \frac{E_{out}}{A_T E_{in}} = \frac{1}{\beta E_{in}} \ln \left\{ 1 + G_{To} \left[ \exp(\beta E_{in}) - 1 \right] \right\}. \quad (21)$$

Eq. (21) is plotted in Figure 3 on a log/log scale with  $G_{T0}$  values of  $10^6$ ,  $10^7$ ,  $10^8$ , and  $10^9$ . Figure 3b is simply an expanded view of Figure 3a. The left-most zero-slope portion of each curve represents the small signal region where Eq. (20) is a good approximation for  $E_{out}(t)$ . Eq. (19) for  $E_{out}(t)$  is valid almost everywhere on the plots, only causing significant error if  $\beta E_{in}$  exceeds 0.1. Typical values for  $\beta$  in the amplifier configurations we will consider are 10-100  $J^{-1}$ . Note that the energy gain of these high-gain multiple-pass amplifiers is saturated for very low input energies. For example, if  $\beta = 100 J^{-1}$  and  $G_{T0} = 10^9$ , which are not unreasonable parameters for a well designed four-pass amplifier, the gross energy gain,  $G_E$ , is reduced from  $10^9$  for extremely small input energies, to  $\sim 6.9 \times 10^6$  with only 10 nJ of input energy. Since  $G_E$  is defined as  $E_{out}/A_T E_{in}$ , the more useful net energy gain  $G_u$ , defined as  $E_{out}/E_{in}$  is simply  $G_u \equiv A_T G_E$ . If, for our example,  $A_T \sim 1$ , the 10 nJ input would result in an output energy of  $\sim 69$  mJ. This output energy is independent of the duration of the 10 nJ input pulse as long as the assumptions leading to Eq. (17) are not seriously violated.

### Extraction Efficiency

The total gross extraction efficiency of the amplifier is given by

$$\eta = E_{exI}/E_{stored} \simeq \frac{1}{A_n E_{stored}} (E_{out} - A_T E_{in}) \quad (22)$$

where Eq. (15) was used for  $E_{exI}$ . Using Eq. (17) for  $E_{out}$  and Eq. (5) for  $E_{stored}$ , we obtain

$$\eta = (\ell n G_{T0})^{-1} \left\{ \ell n \left[ 1 + G_{T0} \left[ \exp(\beta E_{in}) - 1 \right] \right] - \beta E_{in} \right\} \quad (23)$$

The attenuation,  $A_n$ , that is present after the final pass through the amplifier, reduces the useful extraction efficiency,  $\eta_u$ , by a factor of  $A_n$ , i.e.,  $\eta_u = A_n \eta$ . Therefore, for maximum efficiency,

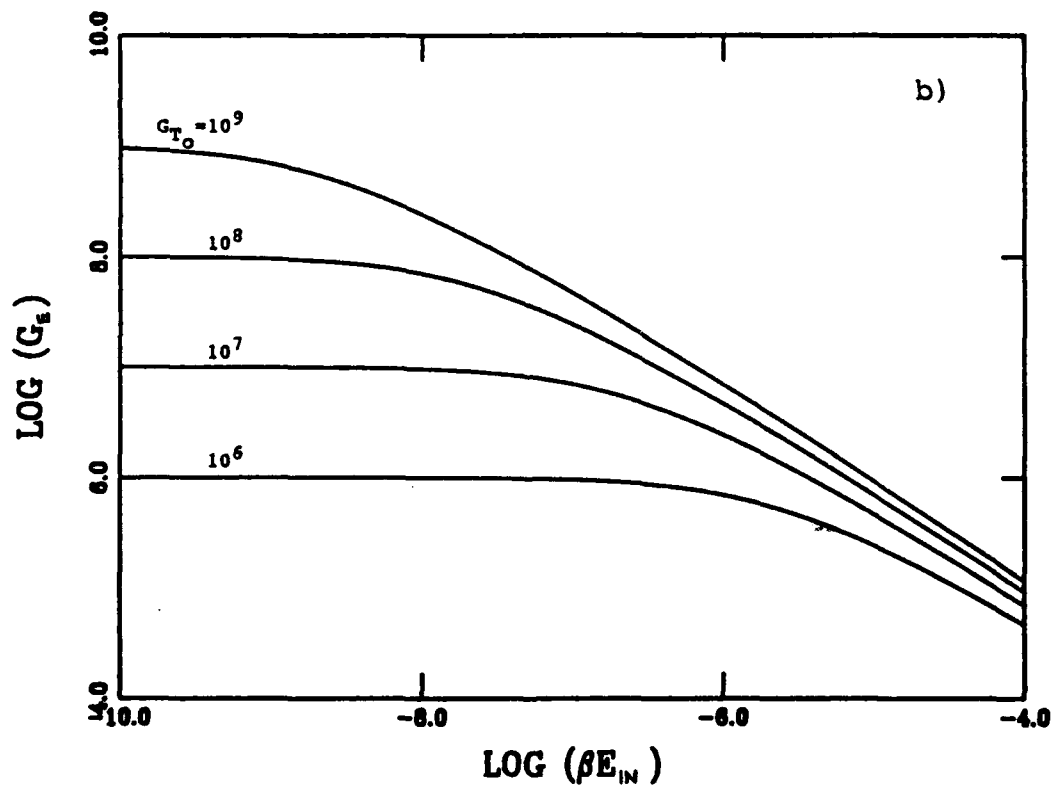
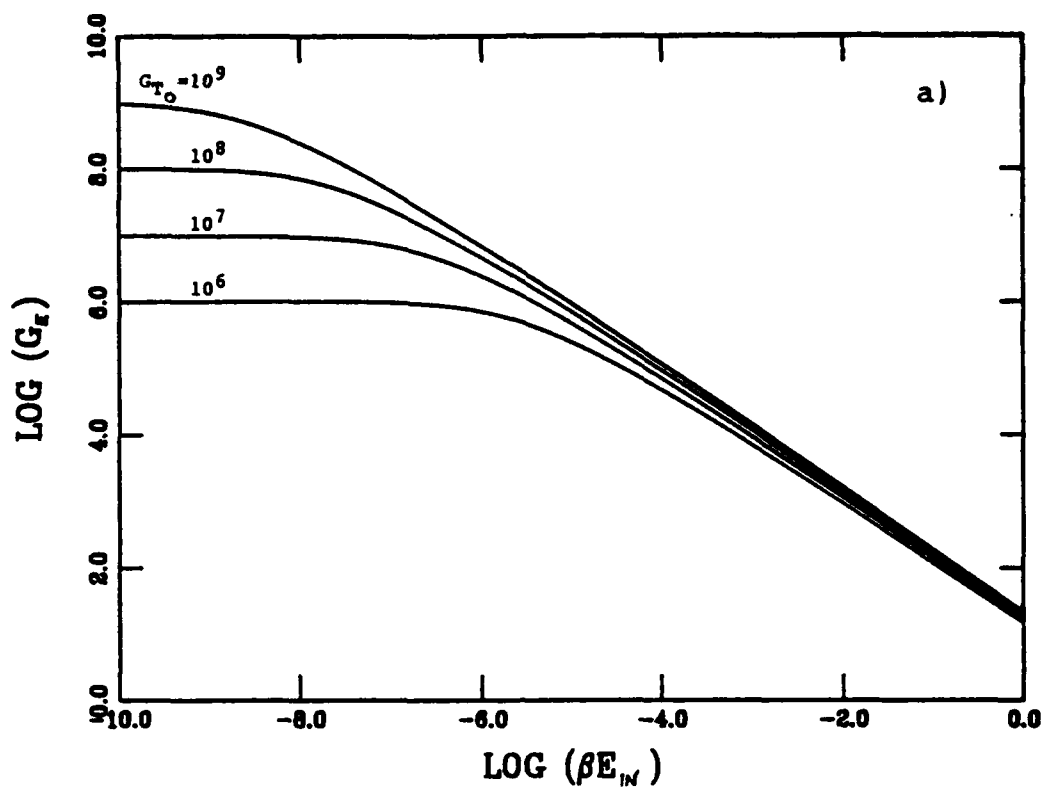


Figure 3a. Gross energy gain versus normalized input energy for four values of small-signal gain  $G_{T_O}$ . Figure 3b is an expanded view of 3a.

it is very important to maximize  $A_n$ , i.e., minimize the loss after the final pass through the amplifier. Eq. (23) is plotted in Figure 4a with a log abscissa and a linear ordinate for  $G_{T0}$  values of  $10^6, 10^7, 10^8$ , and  $10^9$ . Figure 4b is an expanded view of Figure 4a.

Eq. (23) gives the expected values in the limits of both large and small inputs. If  $E_{in}$  is very large so that  $e^{\beta E_{in}} \gg 1$ , Eq. (23) collapses to unity, as expected for a fully saturated amplifier. In the limit that  $E_{in}$  is very small, so that both  $\beta E_{in}$  and  $G_o \beta E_{in}$  are much less than one, Eq. (23) collapses to

$$\eta = \frac{1}{A_n} \frac{A_T G_{T0} E_{in}}{E_{stored}}, \quad (24)$$

which is the expected unsaturated small-signal result. (Remember that  $\eta_u = A_n \eta$ .) All of the cases we will consider for the Nd:YAG preamplifier fall in the region of Figure 4 where  $\beta E_{in} \ll 1$  and  $G_{T0} \beta E_{in} \gg 1$ . In this region Eq. (23) is given by,

$$\eta \sim 1 + \ln[\beta E_{in}] - \ln[G_{T0}] \quad (25)$$

An interesting question to answer is: for what value of the input energy is a fraction  $F$  of the energy stored in the mode volume extracted? In the region where Eq. (25) is valid, this is simply given by

$$E_{in} = \left[ \beta G_{T0}^{1-F} \right]^{-1}. \quad (26)$$

For the example provided earlier where  $\beta = 100 \text{ J}^{-1}$  and  $G_{T0} = 10^9$ , half of the energy stored in the mode volume is extracted when the input energy is only 316  $\mu\text{J}$ . If  $A_T = 1$ , these values for  $\beta$  and  $G_{T0}$  imply that the energy stored in the mode volume is

$\sim 200 \text{ mJ}$   $\left[ E_{stored} = \frac{A_T}{\beta A_n} \ln G_{T0} \right]$ . Thus, the input energy of only 316  $\mu\text{J}$  produces an output energy of  $\sim 100 \text{ mJ}$ .

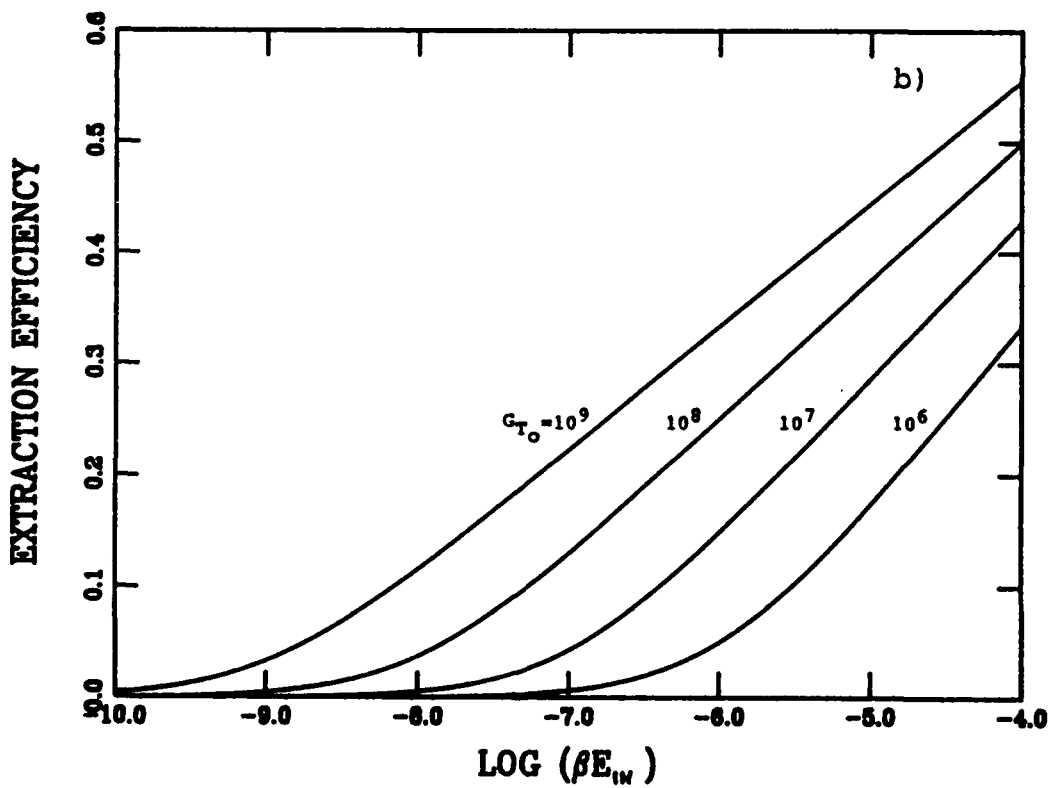
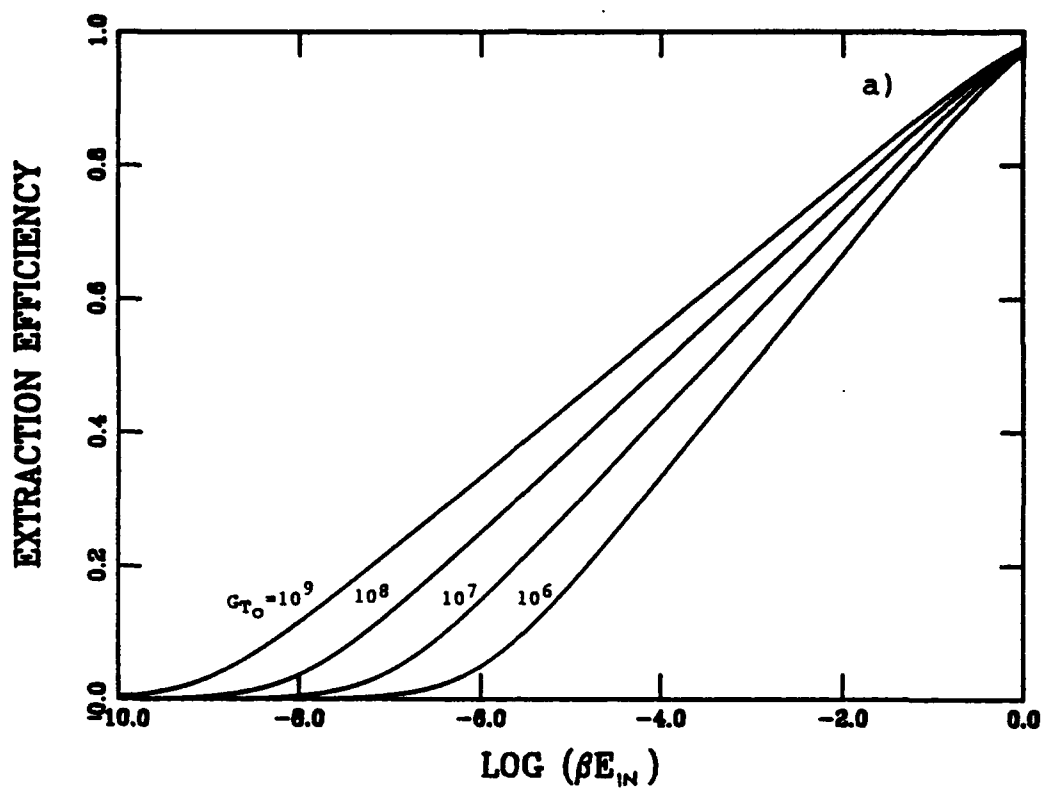


Figure 4a. Total gross extraction efficiency versus normalized input energy for four values of small-signal gain. Figure 4b is an expanded view of 4a.

### Output Power

Another useful expression is the output power one obtains as a function of time. Using Eqs. (15) and (17) in Eq. (14) we obtain

$$P_{out}(t) = P_{in}(t) A_T \left\{ 1 - \left[ 1 - G_{T0}^{-1} \right] \exp \left[ - \beta E_{in}(t) \right] \right\}^{-1}. \quad (27)$$

If  $E_{in}$  is very large, such that  $e^{-\beta E_{in}} \ll 1$ , Eq. (27) gives the expected strongly saturated result [i.e.,  $P_{out}(t) = A_T P_{in}(t)$ ]. In the limit of very small  $E_{in}$  so that  $\beta E_{in} \ll 1$ , Eq. (27) is approximated by

$$P_{out}(t) = \frac{A_T G_{T0} P_{in}(t)}{1 + G_{T0} \beta E_{in}(t)}. \quad (28)$$

If, in addition to  $\beta E_{in}$  being  $\ll 1$ , we are also in the region where  $G_{T0} \beta E_{in} \ll 1$ , the expected unsaturated small signal result is obtained, i.e.,  $P_{out}(t) = A_T G_{T0} P_{in}(t)$ . In the region where  $\beta E_{in}$  is small but  $G_{T0} \beta E_{in} \gg 1$ , we obtain

$$P_{out}(t) = \frac{A_T}{\beta E_{in}(t)} P_{in}(t) \quad (29)$$

Eq. (29) is valid for many of the cases of interest here. Note that Eq. (29) cannot be used to describe the pulse evolution until after the input energy is large enough so that  $G_{T0} \beta E_{in} \gg 1$ .

The gross power gain, defined as the ratio of the power of the amplified beam at the output to that which would be present at the output if the amplifier gain were one, is given by

$$G_p(t) = \frac{P_{out}(t)}{A_T P_{in}(t)} = \left\{ 1 - \left[ 1 - G_{T0}^{-1} \right] \exp \left[ - \beta E_{in}(t) \right] \right\}^{-1} \quad (30)$$

The net power gain, defined as  $P_{out}(t)/P_{in}(t)$ , is simply  $A_T G_p(t)$ .

Figure 5 shows a plot of  $G_p$  vs  $\beta E_{in}$  on a log/log scale for  $G_{T0}$  values of  $10^6, 10^7, 10^8$ , and  $10^9$ . Figure 5b is an expanded version of Figure 5a. The left-most region where the slope is zero is the small signal region where the gain is unsaturated. The region where the slope of the curves is constant and equal to -1 is where Eq. (29) is valid. Note that as predicted for this region, the power gain is independent of the small signal gain. If we go back to our example where  $\beta = 100 \text{ J}^{-1}$  and  $G_{T0} = 10^9$ , an input pulse whose energy is 10 nJ would result in a saturated gross power gain at the end of the pulse of  $G_p \sim 1 \times 10^6$ . Thus, if the 10 nJ input pulse were square, this large reduction in gain would result in severe distortion of the pulse shape.

In the following, we discuss pulse distortion in more detail and describe techniques which can be used to produce the desired output pulse shape.

### Pulse Shape Distortion

To illustrate the distortion that occurs in multiple-pass high-gain amplifiers, we consider the following example which uses parameters similar to those of our 3-pass amplifier configuration (discussed in Section 5). Figure 6 shows the input pulse we use for illustration. It rises and falls linearly between zero input power and the maximum input power of 48 mW in 225 ns. The full-width half-maximum (FWHM) duration of the flat-topped input pulse is 3.9  $\mu\text{s}$ .

Eq. (28) can be used to calculate  $P_{out}(t)$  for this input pulse since  $\beta E_{in} \ll 1$  at all times. Figure 6 shows output power profiles for  $G_{T0} = 4 \times 10^6$ ,  $A_T = 0.16$ , and for different values of the parameter  $\beta$ . Since  $\beta$  is inversely proportional to the mode volume in the gain medium  $\left[ \beta = \frac{A_T}{A_n} \frac{nL}{V} \frac{1}{F_{sat}} \text{ where } F_{sat} = \frac{hv}{\sigma} \right]$ , one way to change  $\beta$  in a given experimental situation is to change the mode volume. Note the increasing gain saturation as  $\beta$  is increased. The resulting full-width half-maximum duration of the output pulse is reduced to  $\sim 300 \text{ ns}$  when  $\beta = 130 \text{ J}^{-1}$ . If

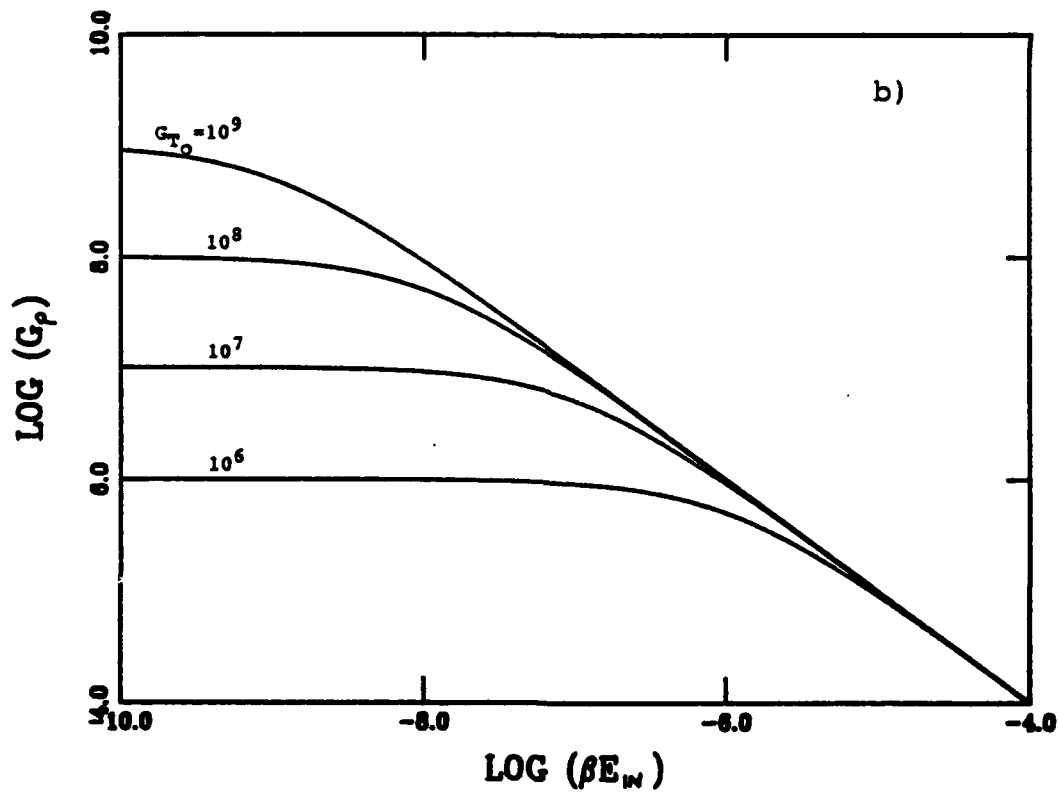
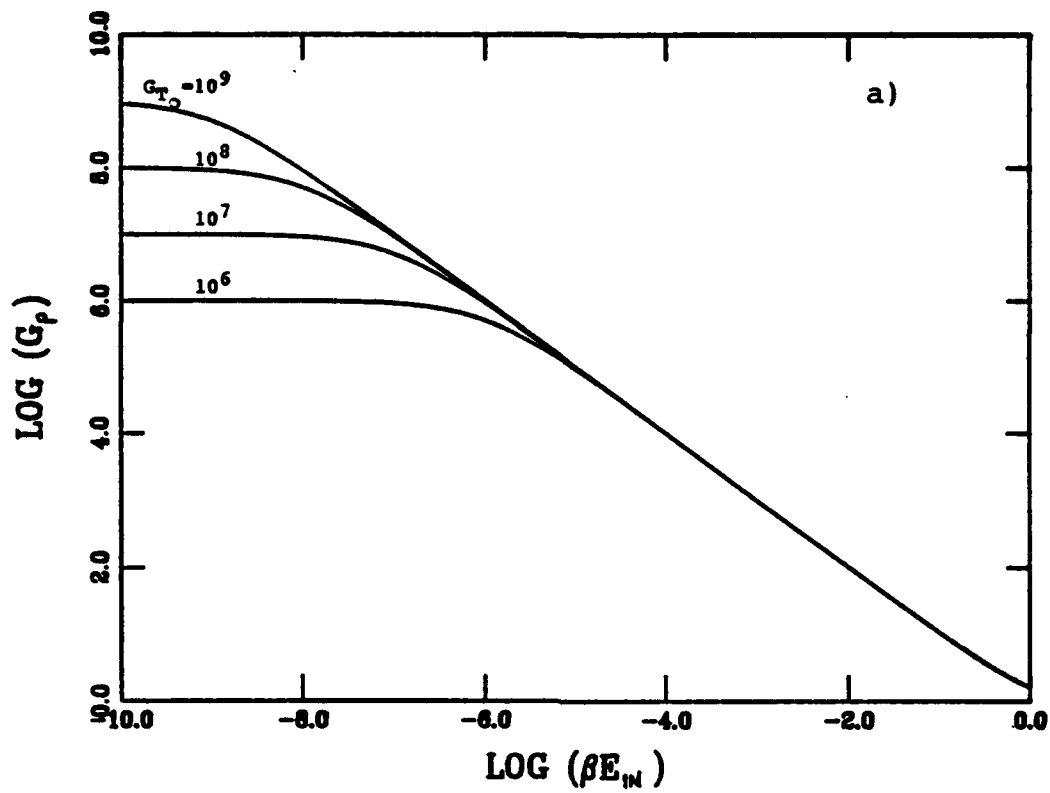


Figure 5a. Gross power gain versus normalized input energy for four values of small-signal gain. Figure 5b is an expanded view of 5a.



# Input/Output For 3-Pass Amplifier

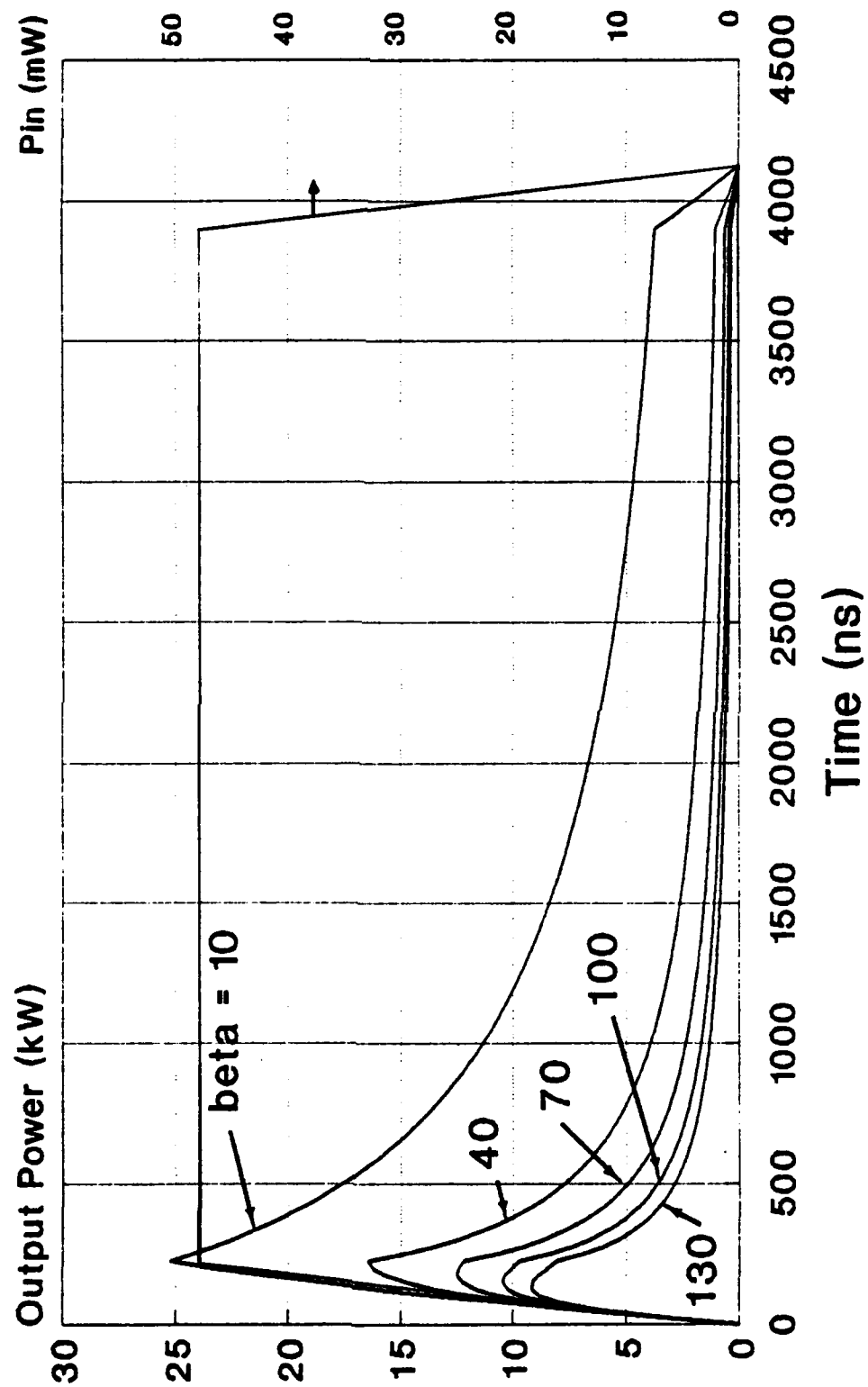


Figure 6. Calculated output power versus time, illustrating gain saturation.

such severe shortening of the output pulse is unacceptable, the input pulse can be shaped so as to counteract the gain saturation and produce the desired output.

The input pulse shape required to produce a temporally flat-topped output can easily be obtained in cases where Eq. (28) is valid (i.e., if  $\beta E_{in} \ll 1$ ). Setting  $P_{out}(t) = P_o$ , where  $P_o$  is a constant, and solving Eq. (28) for  $E_{in}(t)$  and  $P_{in}(t)$  results in

$$E_{in}(t) = \frac{1}{\beta G_{T_o}} \left[ \exp(\beta P_o t / A_T) - 1 \right] \quad (31)$$

$$\text{and } P_{in}(t) = \frac{P_o}{A_T G_{T_o}} \exp(\beta P_o t / A_T). \quad (32)$$

An important point to remember is that the output energy is maximized when the input energy is maximized; see Eq. (17). If the power level of the input source is limited, maximum output energy is obtained, for any given input pulse duration, when the input pulse is flat-topped with the peak power being the maximum available power. Any shaping of the input pulse (using e.g., an acousto-optic or an electro-optic modulator) results in a reduction of the energy of the input pulse and subsequently, a reduction of the output energy from the amplifier. In other words, if you want shaped output pulses, you must pay the price.

#### 4. High Performance Zig-Zag Slab Issues

The long, narrow zig-zag slab is the heart of the multiple-pass preamplifier. The physical shape and configuration of the high-gain slab is uniquely suited to the task of boosting milliwatt-level input signals into the kilowatt regime and beyond. The basic amplifier design we utilize controls unwanted parasitic effects and permits small signal gains of beyond 80 dB in a very compact device. The reader is referred to Refs. 4 and 9 for a detailed discussion of the merits of the long narrow slab geometry as compared to other geometries when high gain

performance is desired. Ref. 9 also provides a detailed discussion of the fabrication tolerances on the slab surfaces if near-diffraction-limited output beams are desired. These same physical geometry characteristics which permit very high gain and multiple-pass amplification do, however, place extremely high demands on the flatness and polish of the high aspect ratio (width-to-length) piece.

Originally, we anticipated that during the Phase I effort the most highly qualified vendor would be identified and contracted with to produce a new, very low distortion Nd:YAG slab to our specifications. ZYGO Corporation (Middlefield, CT) was identified to be the most competent source for providing the piece, and a detailed quotation was solicited from them and several other possible vendors (a more detailed description of the chosen vendor's approach to this problem and cost is given in Section 4.1). Inherent in their approach, however, is the need to purchase a large, very high quality Nd:YAG slab blank, and an overall delivery time which was incompatible with the needs of the Phase I SBIR effort. Early in the project, we decided to pursue two alternatives which would result in a slab of higher quality than was then available, and would broaden our knowledge of slab fabrication tolerances versus performance.

The first alternative involved contracting with the original vendor of our existing slab (Litton/Allied; Charlotte, NC) to refigure and polish that same piece. This approach had the advantages of low cost, high-quality material already in-house, and a turnaround time compatible with evaluating the newly-polished performance in detail during the contract. Table 1 provides a synopsis of the desired slab specifications, compared to the values actually achieved for the original slab and the refigured slab (refer to Figure 1 to identify specific surfaces). A clear priority was placed on minimizing the total transmitted wavefront distortion of a 15-bounce TIR path through the slab, and as can be seen from the table, this distortion was more than halved compared to the original condition. Figure 7 shows the interferograms of the transmitted wavefront distortion

Table 1. Table of original CTI slab surface and distortion values, specifications for refiguring, and refigured slab values.

QUANTITY	DESIRED SPEC	ACTUAL VALUE	
		ORIGINAL	REFIGURED
Mid-Point Length (mm)	104.0 $\pm$ 1.0	105.4	105.2
Height (mm)	4.0 $\pm$ 0.1	4.02	3.85
Width (mm)	4.1 $\pm$ 0.1	4.18	4.18
End Angles (degrees)			
E1	31.25 $\pm$ 0.25	31.0	31.02
E2	3.25 $\pm$ 0.25	31.0	31.05
End Flatness (waves)			
E1	< 0.05	0.06	0.09
E2	< 0.05	0.03	0.096
Overall Pump Face Flatness (waves)			
P1	< 0.5	0.98	1.92
P2	< 0.5	-NA-	2.38
Local Pump Face Flatness (waves)			
P1	< 0.02	-NA-	0.07
P2	< 0.02	-NA-	0.08
Parallelism (seconds of arc)	< 10	-NA-	1.8
Full Aperture Transmitted Wavefront Distortion (waves) (15 TIR Path)	< 0.25	0.784	0.367

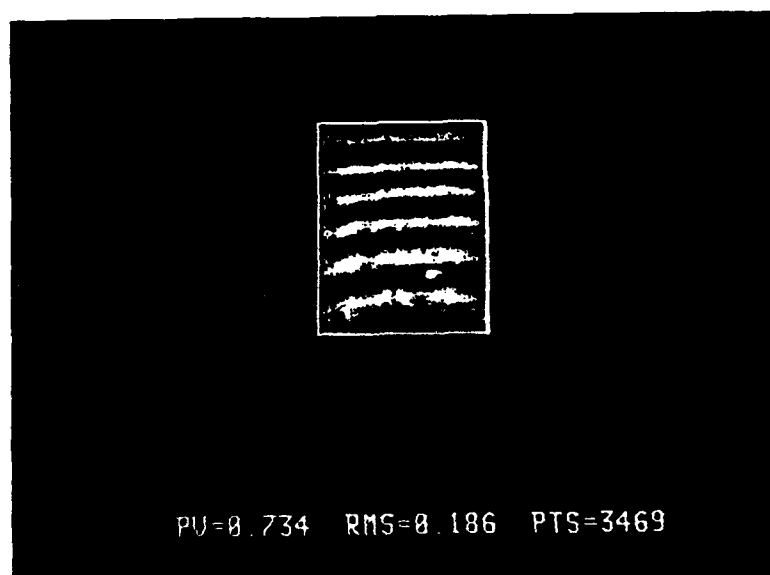
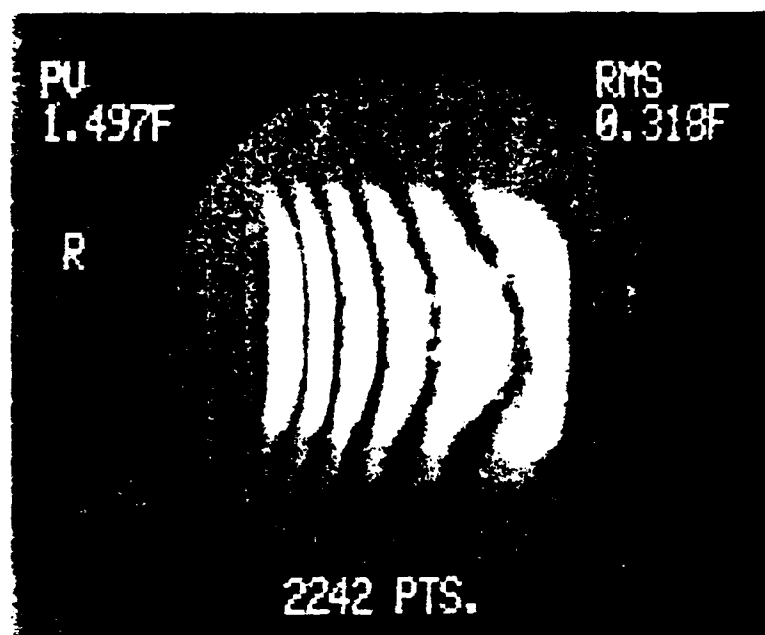


Figure 7. Transmitted wavefront distortion for CTI 4 mm-wide multi-pass slab. TOP: Original condition prior to refiguring. Bottom: Condition after refiguring.

experienced when 633 nm light makes a double 15-bounce pass through the slab. The interferograms were made by Litton/Allied personnel using a ZYGO Mark II interferometer. The piece was essentially "hand figured" to produce compensating curvature on the opposing pump faces P1 and P2; in fact, as shown in Table 1, some actual surface flatness was sacrificed on all critical surfaces in order to reduce the total transmitted distortion. This effective but tedious technique is expected to be avoided in the ZYGO approach described later. Nevertheless, slab performance was, in fact, greatly improved upon the original slab conditions, and proved to give high enough performance to conduct the subsequent laboratory tests of near-diffraction-limited beam amplification (described in Section 5).

The second alternative we investigated was the loan of two Nd:YAG amplifier slabs from Stanford University. We arranged with Stanford to send us two slabs, having dimensions of 4x4x95mm and 4x8x95mm. The principal investigator on this project conducted earlier experiments with the single-wide slab and found its passive beam quality to be quite high. The purpose of obtaining the 4x8x95 mm double-wide slab was to investigate the possibility of using one side (4 mm wide) as the preamplifier and using the other side as a saturated amplifier. If the double wide slab produced sufficient gain, this single hybrid preamplifier/amplifier could be used to boost the pulse energy from 10 nJ, 1- $\mu$ s input pulses to an output energy of several hundred mJ. In comparison the single wide preamplifier (or the preamplifier side of the double wide hybrid device) is more likely to produce ~25-50 mJ of output from the same level of input. Of course the pump power required for the double wide slab would be greater, by a factor of two or more.

Preliminary measurements made at Stanford University indicated that the gain obtained from the double wide configuration was considerably less than that obtained from the single wide configuration. Since the Stanford investigators did not express confidence in their measurements, our intent was to make the gain measurements ourselves. Time constraints and a

steady flow of positive results using the refigured CTI slab preempted the laboratory evaluations planned for both the single and double-wide pieces. CTI anticipates making the small-signal gain measurements using the 8 mm-wide slab in the near future and will forward a copy of those results to the scientific officer of this contract when available.

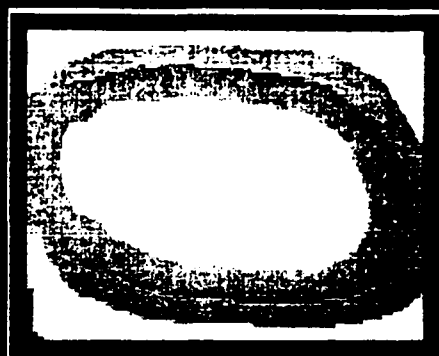
In any event, the Stanford slabs were sent to ZYGO Corp. for detailed interferometric analysis of surface figure and zig-zag transmitted wavefront distortion. Figure 8 shows the resulting interferograms. For both slabs, the distortion is greater than desired, with the peak-to-valley distortion being 1.01 waves for the 4-mm wide Stanford slab and 0.67 waves for the 8-mm wide slab. Note that if one stays away from the extreme edges, the distortion is only 0.58 and 0.38 waves for the 4- and 8-mm wide slabs, respectively. Also note that the total wavefront distortion of the beam can be very low if the beam diameter is very small. In particular for the single wide Stanford slab a 1mm diameter 1064 nm wavelength beam centered in the slab input aperture would experience  $<0.008$  waves of distortion (peak to valley at 1064nm) on making a 15-bounce pass through the slab. Similar results are obtained with the CTI slab used for the experiments described in Section 5. This is very relevant since for the first 2 passes (and to some degree for the 3rd pass) through the amplifier the intensities for beam diameters of 1mm or less are very low and do not saturate the gain. Thus the wavefront distortion accumulated during the first 2 or 3 passes can be kept quite low. Of course, for efficient extraction of the energy stored in the amplifier, the beam diameter in the final pass must be comparable to the slab width/thickness.

Figure 8 shows that the distortion introduced by the 4-mm wide Stanford slab is, to a large degree, very smooth. In theory, a phase plate or the proper combination of spherical and cylindrical lenses could remove most of the phase distortion. The principal investigator of this contract has used this 4-mm wide slab in past efforts and has found that a pair of spherical lenses between each pass through it can be very effective in

\*\*\* WAVEFRONT \*\*\*

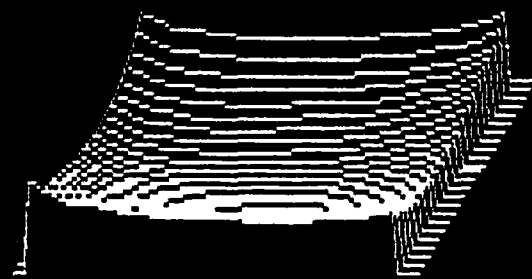
16-NOV-1989/10:58:51

Part ID : ZIGZAGSLAB 15 bounce  
 Serial # : 4mmx4mmx105mm  
 Analysis : phase  
 F/NO : plano Fast : off  
 Averages : 4 Trim : 2  
 Calibrate: ON AGC : ON  
 Wave Out : 0.6328 Scale: 0.50  
 Reference: none  
 Remove : TLT



-1.01  
 -0.86  
 -0.72  
 -0.58  
 -0.43  
 -0.29  
 -0.14  
 -0.00

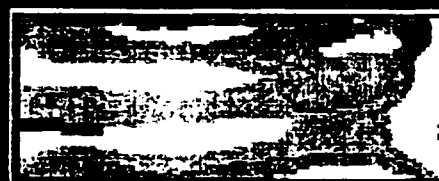
PV : 1.008 PTS : 2591  
 RMS : 0.192



\*\*\* WAVEFRONT \*\*\*

17-NOV-1989/10:09:04

Part ID : ZIGZAG 15 BOUNCE  
 Serial # : 4mmx8mmx105mm  
 Analysis : phase  
 F/NO : plano Fast : off  
 Averages : 4 Trim : 1  
 Calibrate: ON AGC : ON  
 Wave Out : 0.6328 Scale: 0.50  
 Reference: none  
 Remove : TLT



-0.672  
 -0.576  
 -0.480  
 -0.384  
 -0.288  
 -0.192  
 -0.096  
 -0.000

PV : 0.672 PTS : 5219  
 RMS : 0.089

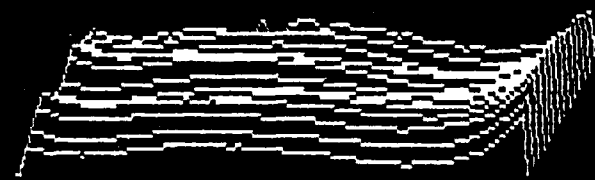


Figure 1. 2D and 3D wavefront distortion for standard multi-

Figure 2. 2D and 3D wavefront distortion for standard multi-



controlling the total multiple-pass wavefront distortion. The distortion introduced by the double wide slab, although smaller in peak-to-valley magnitude, is more random in nature and would be harder to control. The peak-to-valley distortion experienced by a 633 nm beam, making a 17-bounce pass through the refigured CTI 4x4x105-mm slab, is  $\sim 0.37$  waves peak-to-valley and similar to the 4-mm wide Stanford slab; the distortion is relatively smooth and was effectively compensated by spherical and cylindrical optics (see Section 5).

#### 4.1 Recommended Slab Fabrication Procedure and Estimated Cost

A truly high quality (diffraction-limited) slab is of course the desired goal for future flashlamp- and diode-pumped versions of this amplifier. As will be seen in Section 5, this goal was approached with the refigured CTI slab, but even higher performance will be required for the demanding long-range, all-solid-state lidar applications envisioned.

Of all vendors contacted, ZYGO Corporation exhibited the most confidence in producing long and narrow Nd:YAG slabs having specifications as shown in Table 1. Their proposed approach was provided to us in considerable detail and was evaluated to be a highly rigorous, relatively low-risk technique to achieve or exceed the desired minimization of wavefront distortion.

The first step in the fabrication process is the procurement of a very high quality  $\sim 4.5 \times 12 \times 120$  mm Nd:YAG blank. This very wide blank provides large area pump face "working surfaces" (i.e., the length to width aspect ratio is reduced to  $\sim 10$  to 1) during the critical polishing phase and is key to their approach, compared to other vendors contacted. To insure that the finished slabs meet the required 15-bounce wavefront distortion specification, the bulk material used to make the 12 mm wide blank must be of the highest quality, with the transmitted wavefront distortion through the blank being considerably less than 0.25 waves peak to valley at  $\lambda = 633$  nm. It should be noted that the smaller blank used for the original CTI slab had bulk distortion of only  $0.065 \lambda$ , indicating that the necessary levels

are attainable.

The vendor proposes to polish flat and parallel the two opposing 12 mm wide by 120 mm long faces. With surfaces of this relatively large area to work with, they anticipate no trouble from bending or stress. After polishing these wide faces and the opposed 31° end faces, the piece will be cut lengthwise into one or more 4-mm wide pieces, with interferometry guiding the selection of specific 4-mm regions having the lowest 15-bounce transmitted wavefront distortion. The process described above is expected to result in one and possibly two 4-mm wide slabs. Given high enough quality slab blanks, the vendor fully expects this process to result in the reliable, repeatable manufacture of slabs having  $\lambda/4$  or less total wavefront distortion (peak-to-valley at 633 nm), when undergoing a 15-bounce TIR path through the slab. This corresponds to only  $\sim \lambda/7$  at 1064 nm which implies a high Strehl ratio, particularly if what slight distortion that may still remain is highly regular and hence easily compensated externally.

A good estimate of the cost of one or two high performance slabs can be made based on quotes from the selected vendors in mid-September, 1989:

1) Litton/Allied low-distortion slab blank, 4.5x12x120 mm	\$ 6250
2) ZYGO non-recurring expenses for slab fabrication	2200
3) ZYGO slab fabrication, 1 slab guaranteed to spec.	<u>10,780</u>
	\$19,230

ZYGO rates as a high probability that a second "in-spec" slab will result from the above fabrication process; if so, the cost would be \$2000.

Economy-of-scale principles are expected to apply very positively to the manufacture of the amplifier slab, in quantities beyond ten pieces each; the efficient production of such slabs will benefit greatly from the knowledge gained in the first pieces produced. In addition, CTI fully expects in the near future, to answer important questions about the viability of

wider (and hence lower aspect ratio) slabs for the high-gain multi-pass application. This information could, in turn, positively influence the cost and ease of slab fabrication and overall amplifier efficiency.

## **5. Results of Experimental Evaluation**

### **5.1 Description of Multiple-Pass Amplifier System**

We designed a laser head to pump 4mm-wide multiple-pass slabs at relatively low average power on a previous contract (see "Acknowledgments" at the beginning of this report). This subsystem served well as a test-bed for beam characterization and higher power studies during this effort. The central 76 mm of the slab is directly pumped by the light from a single xenon flashlamp. A diffuse-reflecting close-coupled pump chamber consisting of a samarium-doped dual-bore flow tube overcoated with barium sulfate, couples the flashlamp light to the slab. We obtained the barium sulfate overcoated flow tube from a commercial vendor (KIGRE, Inc., Hilton Head, SC) and designed the end connectors ourselves. The slab is supported in the pump chamber at each end using the two non-optical surfaces of trapezoidal shape, so that all four optical surfaces and the central 76 mm of the two non-optical surfaces are surrounded by water only. The end connectors are designed so that a thin-layer ( $\sim 0.6$  mm thick) of water flows across the entrance and exit end faces of the slab. The central 76 mm of the top, bottom, and two sides of the slab are in contact with a highly turbulent, longitudinal flow of cooling water. The pump chamber was designed so that the non-optical sides of the slab can be thermally insulated from the cooling water as is normally done in higher aspect ratio slab amplifiers. We found that in practice such insulation techniques were unnecessary in our unity-aspect ratio slab amplifier, even when operating at the present PRF-defined limits of our flashlamp power supply (12 Hz @ 30 J/pulse, or  $\sim 360$  W loading). Higher PRF's may in fact require insulation to be applied.

A refrigerated water circulator constructed entirely of plastic and stainless steel is used to circulate the deionized water in the amplifier head and to maintain the water temperature at a fixed value (typically  $20^{\circ}\text{C}$ ). The flashlamp used to pump the slab has a 76 mm arc length and a 4 mm bore. The lamp is filled with xenon to a pressure of 450 torr and the envelope is made of cerium-doped fused silica. The power supply and pulse forming network (PFN) used to control the flashlamp is capable of delivering up to 450 W of average power with the maximum pulse energy being  $\sim 110\text{ J}$ . The FWHM duration of the current pulse through the flashlamp is  $\sim 200\text{ }\mu\text{s}$ . The PFN is currently designed to be critically damped at pulse energies near 60 J.

The slab dimensions (given in Table 1) allow up to 5 passes to be made. The number of bounces,  $N$ , the internal angle,  $\theta$ , and the external angle,  $\delta$  (refer to Figure 1), for each of these propagation paths can be calculated using the slab dimensions.<sup>4</sup>

Figure 9 shows an overhead view of the amplifier head and associated optical hardware used during the majority of this experimental effort. An existing CW diode-pumped master oscillator (MO) provides an initial seed source of single-frequency diffraction-limited  $1.06\text{-}\mu\text{m}$  light for the multiple-pass amplifier. This laser typically provides 45 mW CW to the input of the 1st pass of the amplifier. Beam steering periscope P shifts the MO beam up in height and lens  $F_1$  is used to form a beam waist of  $\sim 2\text{ mm}$  diameter ( $1/e^2$  intensity) in the 1st pass of the amplifier slab. A flint glass acousto-optic modulator (AOM) is used in the 1st pass output to "gate out" a square pulse of  $0.2\text{ }\mu\text{sec} - 10\text{ }\mu\text{sec}$  duration for amplification in the successive passes. This AOM also provides an isolation of  $\sim 1\text{ part in }10^4$  when it is in its off state (i.e. the AOM is slightly leaky), which helps to isolate the 1st pass from successive passes. The AOM is followed by a Faraday isolator  $I_1$ , which transmits  $\sim 85\%$  of the forward traveling light and attenuates backward traveling radiation by  $\sim 10^4$ . The concave folding mirror, M, serves as a refocusing optic to compensate beam divergence for injection into the 2nd pass, producing a beam

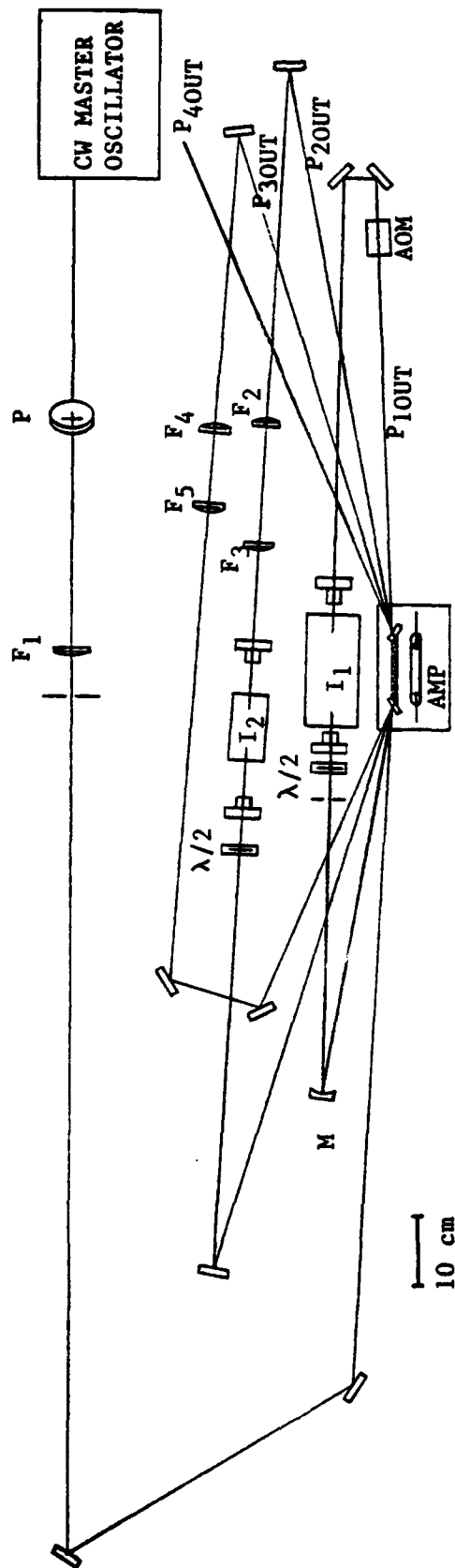


Figure 9. Overhead view of multiple-pass amplifier system.

waist of 1.5 mm diameter.

The output of the 2nd pass is down-collimated by a factor of two by lenses,  $F_2$  and  $F_3$ , and sent through another Faraday isolator  $I_2$ . Lens  $F_2$  is adjusted finely to provide a beam diameter in the 3rd pass of nominally 2.5 mm.

At this point, passive wavefront distortion due to multiple bounces from the faces of the slab has accumulated to an extent that some simple cylindrical correction is desirable. A matched pair of cylindrical lenses,  $F_4$  and  $F_5$ , are used to alter the horizontal divergence and remove most of the wavefront distortion (which is mostly cylindrical in nature). The cylinder lenses produce a round, 2.5 mm diameter beam in the 4th pass.

## 5.2 Multiple-Pass Operation and Gain Characterization

In this section we describe the performance of the system described above under various operating conditions.

### Small-Signal Gain

The gain of the multi-pass amplifier was determined for 2-, 3-, and 4-pass operation (Figure 10). Gain in Figure 10 is defined as the peak output power of a given amplifier pass, divided by the passive (no amplification) output power of the same pass (i.e. gross gain). In each case, the CW signal input from the MO was attenuated with neutral density filters to a level that assured operation in the small-signal regime (i.e.  $G_{To} \rho E_{in} \ll 1$ ; see Section 3.2). In all cases, small-signal gain effectively clamps at a flashlamp energy of about 30 J. This is due to internal parasitic paths and amplified spontaneous emission (ASE), which tends to clamp the population inversion, draining off most of the additional energy when pumped above 30 J. The maximum gain values of 44 dB and 66 dB for 2- and 3-pass operation respectively, are very similar to values recorded in earlier work.<sup>5,6</sup>

As can be seen from Figure 10, this  $\sim 22$  dB/pass behavior continues to hold for 4-pass operation, yielding a small-signal

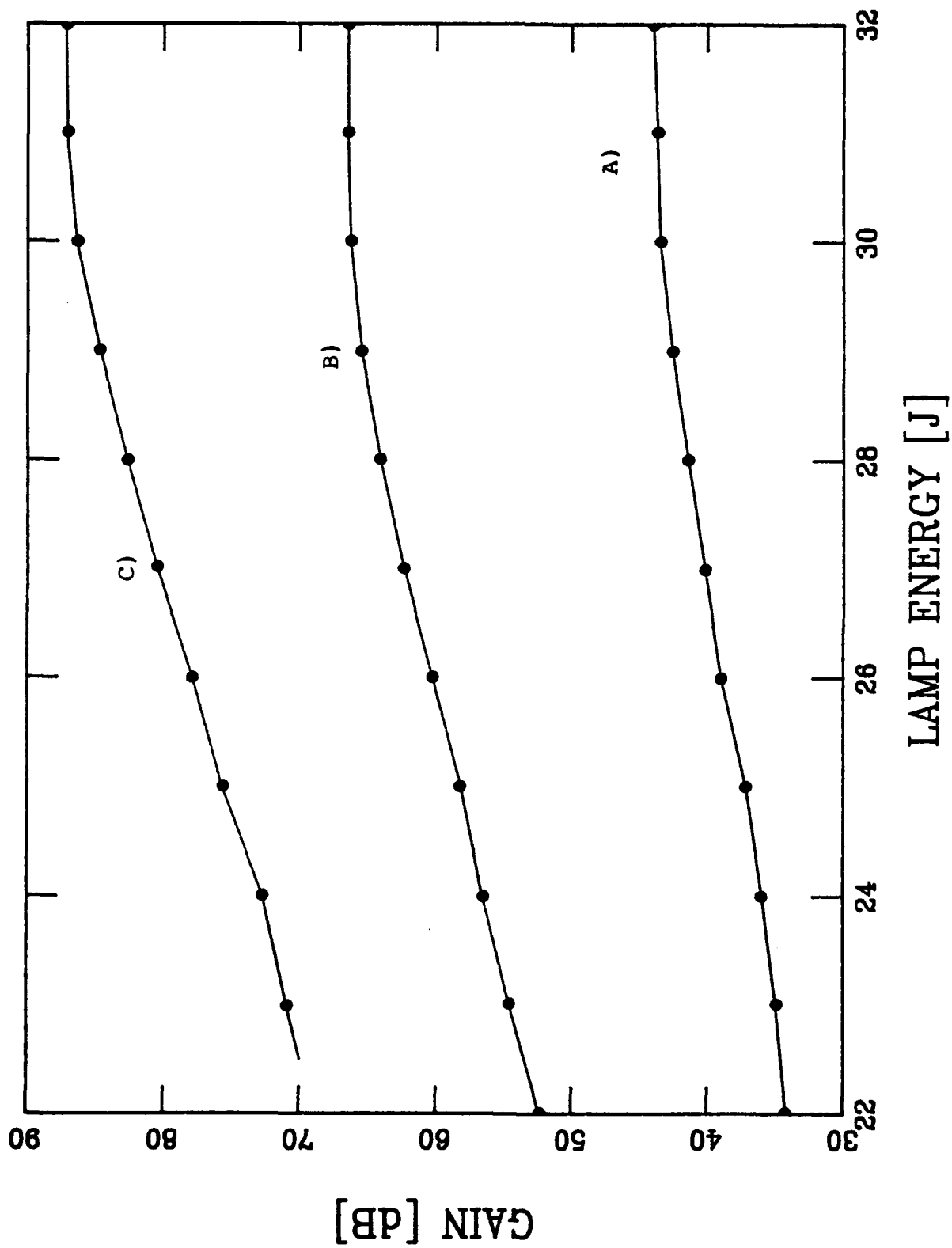


Figure 10. Small-signal gain. A) 2-pass output. B) 3-pass output. C) 4-pass output.

gain of 87 dB ( $\sim 5 \times 10^8$ ), for a flashlamp pulse energy of 31 J. The level of gain persisted for  $\sim 50 \mu\text{s}$  FWHM. This performance is significantly higher and more efficient than the earliest reported work on this type of preamplifier,<sup>4</sup> and represents the highest gain from this device so far seen in our laboratory.

#### Multiple-Pass Pulse Energy Characterization

In the first two passes, the energy density in the amplifier is still in the small-signal regime and very little stored energy is swept out. Significant energy extraction begins in the 3-pass configuration, as shown in Figure 11. A Molectron J-25 pyroelectric joulemeter was used to record output pulse energies with increasing flashlamp pulse energy; five AOM-gated pulsewidths are plotted to show the increase in energy extraction with increasing pulse width. During these measurements the input to the 4th pass was blocked by the joulemeter (see Figure 9). Again, ASE and parasitic oscillation paths inside the slab limit the gain beginning at about 30 J of flashlamp energy. The input signal to the first pass was  $\sim 45 \text{ mW}$ . Note that due to gain saturation the pulse energy does not increase linearly with the pulse length.

ASE and amplified "background" due to imperfect AOM extinction before and after the gated pulse, account for only a very small fraction of the amplified energy in the 3-pass configuration. We have previously measured the effective noise input to the amplifier by placing an aperture in the far field which transmits  $\sim 98\%$  of the amplified beam. The peak power passing through the aperture with no optical input to the amplifier was measured at maximum gain ( $\sim 30 \text{ J}$  pump). The measured power was divided by that gain to find an effective input power. This effective input noise power was found to be less than 100 nW.

Figure 12 shows the relative output power vs time for the 3-pass amplifier pumped with  $\sim 28.5 \text{ J}$  from the flashlamp. The input pulse shape generated by the AOM rises and falls



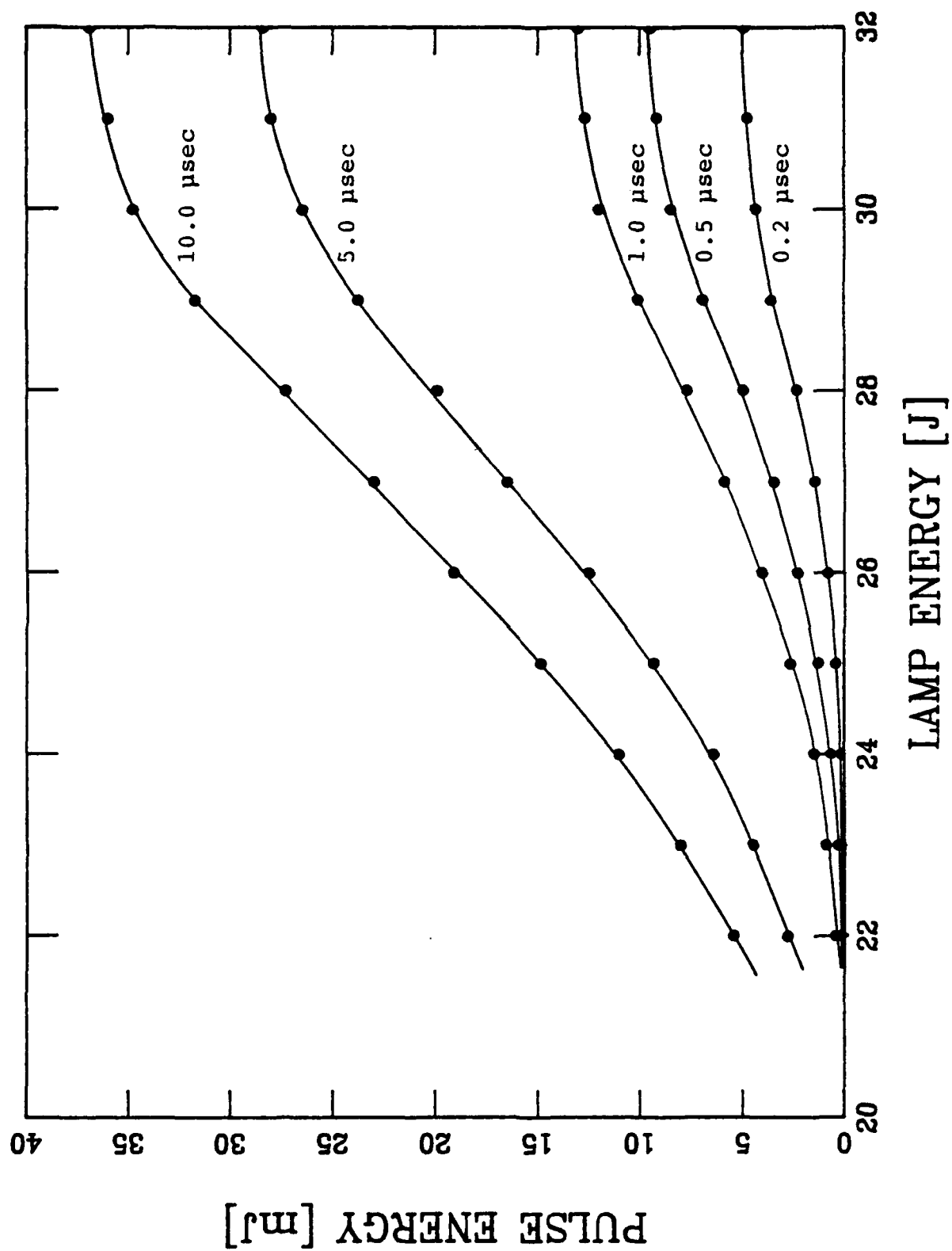


Figure 11. 3 pass pulse energy for five different AOM gate pulsewidths.

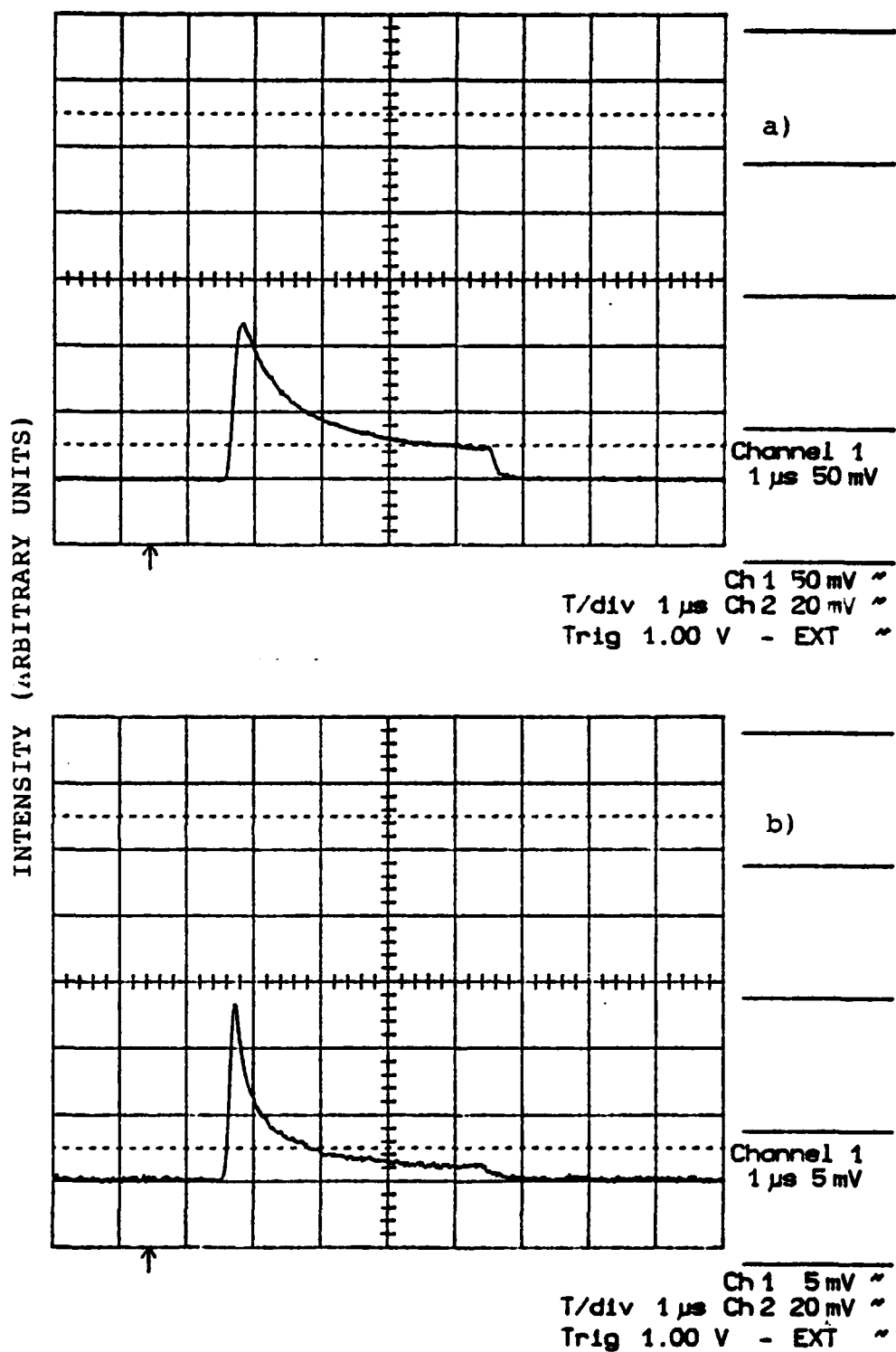


Figure 12 a). 3-pass output pulse shape, beam diameter 2.45 mm @  $1/e^2$ . b) same conditions but beam diameter reduced in 3rd pass to 0.61 mm. Intensity scales differ for the two beam size conditions.

approximately linearly from its peak value to zero in 225 ns. The  $\sim 3.7 \mu\text{s}$  region in between the rising and falling edges is flat-topped (i.e., the FWHM duration is  $\sim 3.9 \mu\text{s}$ ). Figure 12a shows the output when the diameter of the beam in the 3rd pass is  $\sim 2.5 \text{ mm}$  ( $1/e^2$  intensity of Gaussian input). The output energy for this  $3.9 \mu\text{s}$  pulse was  $\sim 20 \text{ mJ}$ . Note the gain saturation (reduced output power) vs time.

Figure 12b shows the output under the same operating conditions except that the 3rd pass beam diameter was changed to  $\sim 0.6 \text{ mm}$ . With this smaller beam diameter, the pulse energy drops to  $10 \text{ mJ}$  due to a more pronounced saturation effect. This agrees reasonably well with the trend shown in Figure 6 which illustrates that as  $\beta$  increases ( $\beta$  is inversely proportional to the mode volume) the saturation effect increases.

Additional energy extraction occurs in the full input-signal, 4-pass configuration. At this level of amplification, the raw pulse energy measured using the joulemeter must be corrected for a spurious effect which adds onto the true pulse energy. This effect is the AOM "off-state" CW leakage noted above. Even though the AOM attenuates the input power by  $\sim 1$  part in  $10^4$  when it is in its "off state," the leakage grows to many millijoules upon 4-pass amplification. Figure 13a shows the 4-pass output when the AOM remains in its "off state" throughout the rise and fall of the gain. Note that the FWHM of this "leakage pulse" approximately matches that of the unsaturated gain (i.e.  $\sim 50 \mu\text{s}$  FWHM). This leakage energy was recorded for the relevant range of lamp energies by removing the gate signal to the AOM amplifier. The energy of these leakage pulses can reach upwards of  $10 \text{ mJ}$  for the higher pump energies ( $>30 \text{ J}$ ). It was found, however, that due to gain saturation by the much higher intensity gated laser pulse, the leakage energy drops essentially to zero immediately after the gated pulse. Figure 13b shows the leakage pulse which results when the gain is saturated by a gated laser pulse which is shown as the large spike leaving the Figure. Thus, to correct the pulse energy values, a significant fraction of the "leakage only" energy

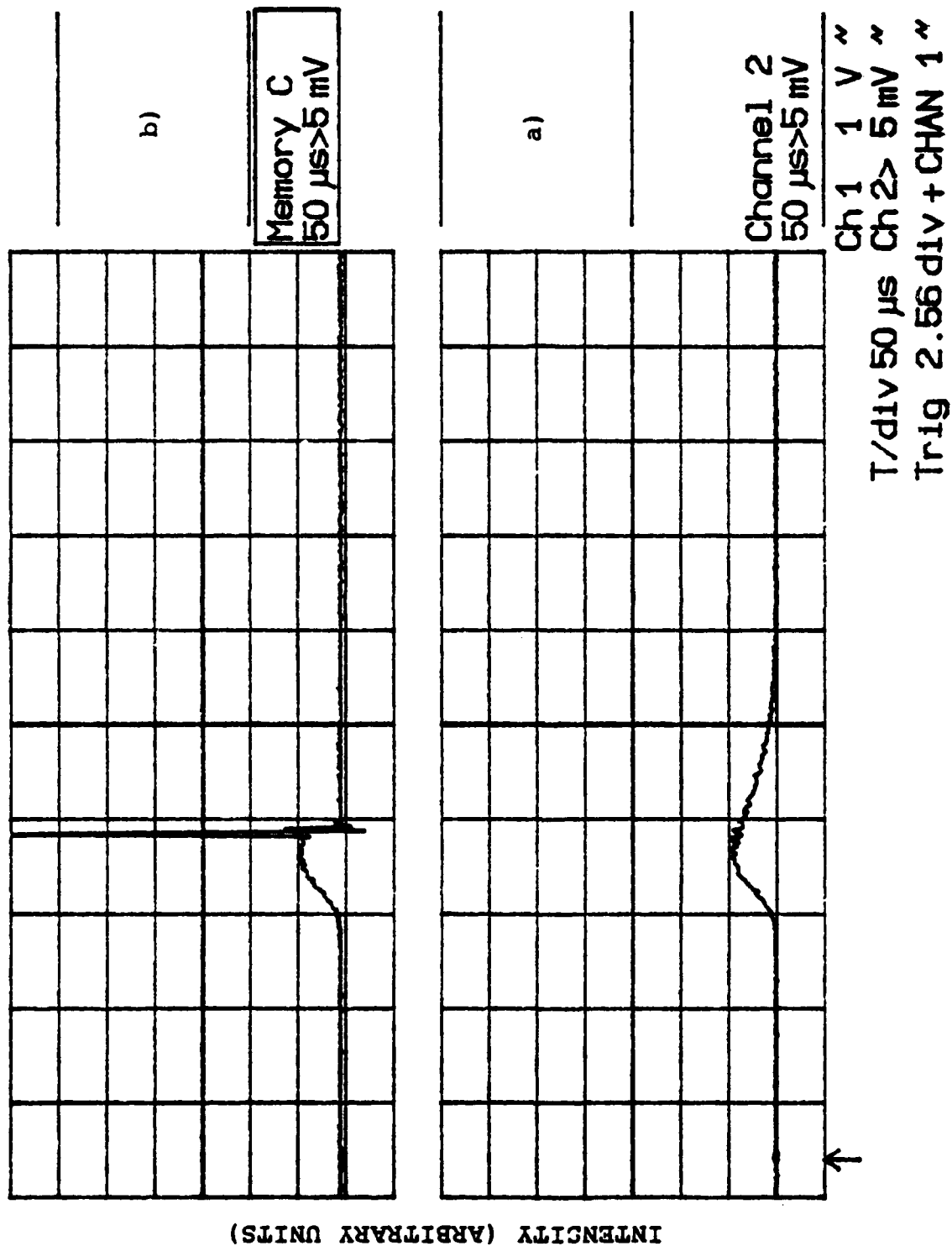


Figure 13. AOM leakage. a) Leakage pulse after 4-pass, 32 J amplification,  $\sim 32$  mJ. b) Leakage energy condition with 1.0  $\mu\text{sec}$  AOM gate pulse; only  $\sim 50\%$  of energy present in a) due to laser pulse gain saturation.

recorded can be thrown out prior to subtracting that energy from the amplified laser pulse values. Moreover, this fraction is lamp energy-dependent (more leakage energy occurs before the AOM gate with increasing lamp energy); hence, a set of data with varying lamp energies similar to Figures 13 a) and b) had to be evaluated individually to produce correction factors corresponding to each laser pulse energy value. Of course, this leakage pulse could be eliminated by using an AOM having a higher on/off ratio. AOM's that have ratios of >70 dB are possible and CTI is currently procuring such devices for use in our 1.06  $\mu\text{m}$  laser radar.

Figure 14 shows the corrected 4-pass output pulse energies with increasing flashlamp pump energy, for five different AOM gate pulsewidths. The input signal power from the M0 was  $\sim 45$  mW. The amplifier is now operating in the saturated regime and efficient stored energy extraction occurs.

Figure 15 illustrates the effect of 4-pass gain saturation on a flat-topped 1  $\mu\text{s}$  input pulse generated by the AOM. Amplifier stored energy extraction is most efficient under these conditions since the input energy is maximized. In laser radar applications the input pulse shape could be modified temporally with acousto- or electro-optical modulators, to compensate the effects of saturation and result in a "flat-topped" output pulse, or any other specific pulse shape desired. Of course, shaping of the input pulse will reduce the energy of the input pulse, which as described in Section 3.2 results in reduced output energy.

An important operating parameter, especially in the 4-pass configuration, is the laser mode diameter in the amplifier slab. The beam size in the 4th pass will affect energy extraction efficiency as well as output beam spatial quality, and a practical trade-off study was conducted to determine an optimum beam "filling factor" for the 4th pass through the slab. Using a 1.0  $\mu\text{sec}$  AOM pulsewidth, four different beam waists were formed in the amplifier and pulse energy vs beam diameter were plotted (Figure 16). These energies are not corrected for AOM leakage.

The smallest beam formed, 1.7 mm diameter at  $1/e^2$ , accessed

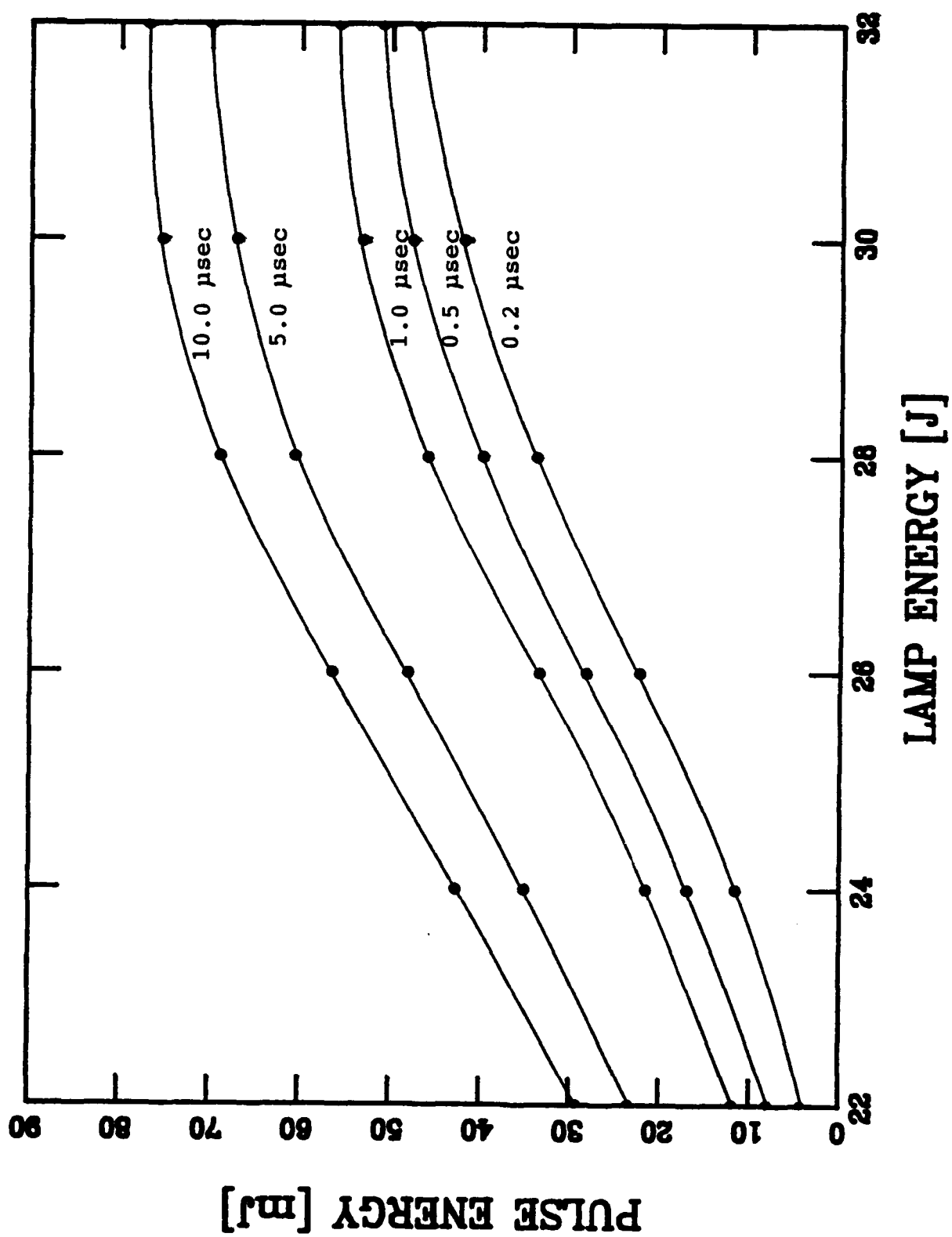


Figure 14. 4 pass pulse energy for five different AOM gate pulsewidths. Energies corrected for AOM leakage level.

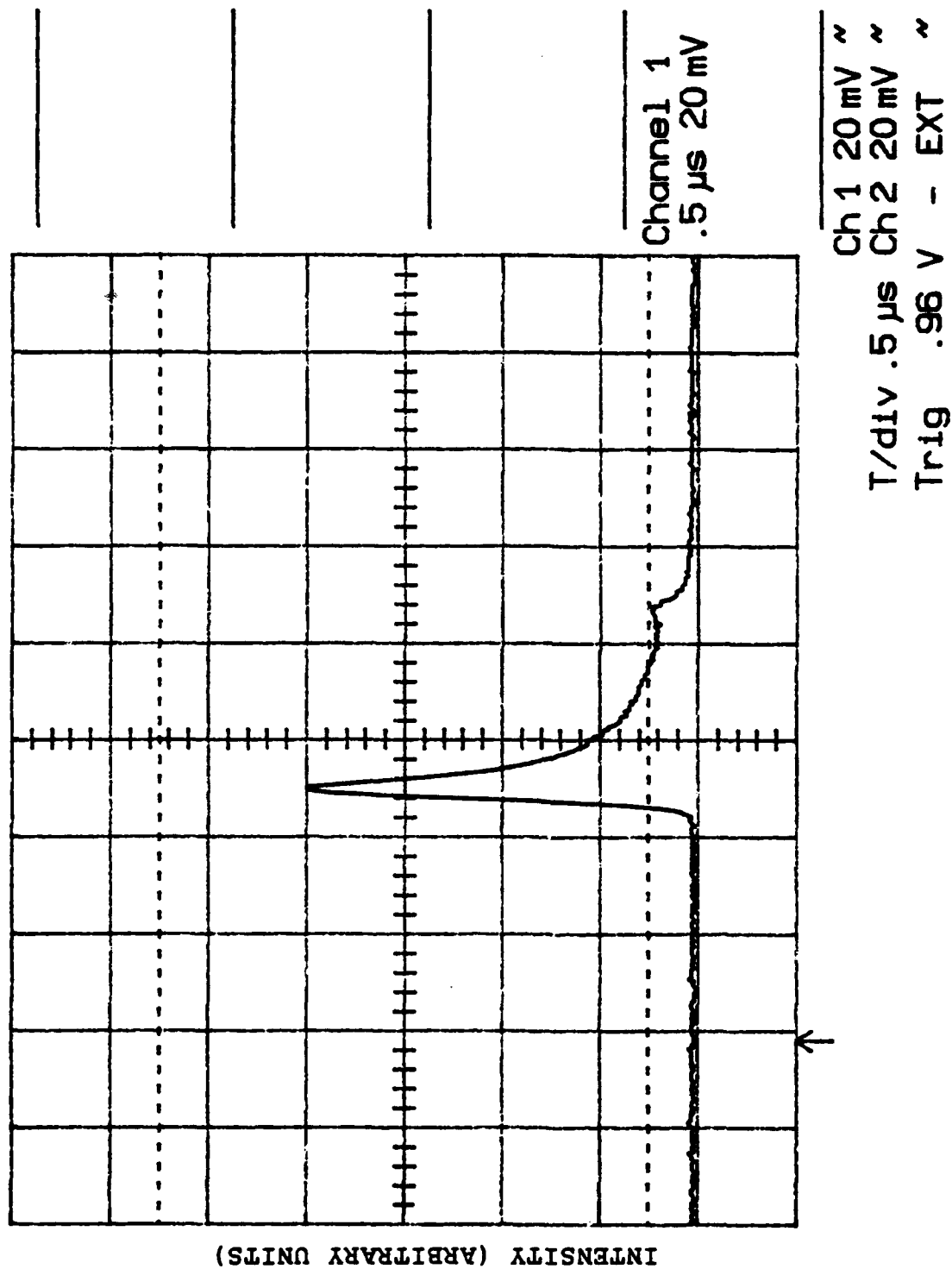


Figure 15. 4-pass output pulse with 1.0  $\mu$ sec AOM input pulse, 32 J flash pump energy. Energy in output pulse 57 mJ.

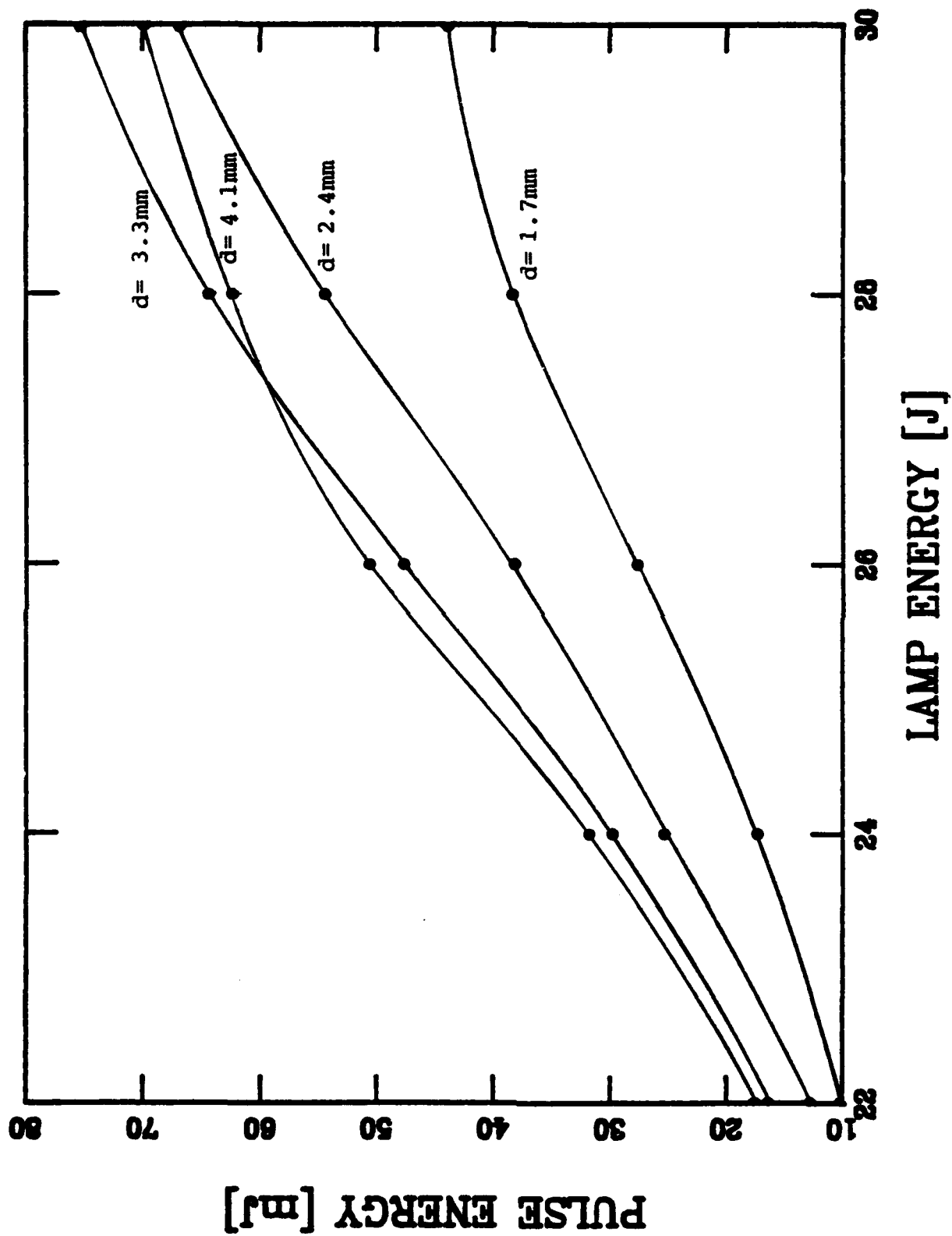


Figure 16. Pulse energy as a function of beam diameter formed in 4th pass. Pulse energy not corrected for AOM leakage energy.



the smallest volume of stored energy and hence produced the lowest output energy. When the diameter was increased to 2.4 mm, an increase of  $\sim 50\%$  is gained in output energy. As the beam size is increased further, the energy gains slow down and diffraction losses begin to build at higher pump levels. This may be due to some filling-in of the wings of the Gaussian beam profile as saturation occurs, and the 4.1 mm beam begins to drop in energy as it more seriously overfills the 4.0 mm square slab aperture, with increasing pumping energy. These data coupled with spatial beam profiling under various operating conditions (described in detail below), led us to perform almost all tests and characterizations using a 2.4 - 2.5 mm diameter 4th-pass beam.

### 5.3 Spatial Beam Quality Evaluations

Central to this Phase I effort was quantitative evaluation of the multi-pass amplifier spatial beam quality under specific operating conditions. High quality near-diffraction-limited beam quality is needed for the laser radar application as well as others. An understanding of the beam distortion during both low and high average power operation is needed before diffraction limited, diode-pumped, high-gain, multi-pass amplifiers can be confidently designed. By simple thermal loading considerations the flashlamp-pumped results obtained here can be used to predict the performance of diode-pumped multi-pass amplifiers. In the following we describe the beam quality measurements.

A linear, 256-element beam profiling diagnostic was developed based on a Fairchild CCD array chip and support electronics. This device was used to make CW and pulsed, passive and amplified beam profile measurements on beam diameters of up to  $\sim 3$  mm. Hard copy records were made using a LeCroy 9400 digital oscilloscope and an HP pen plotter, and with an analog oscilloscope camera. The array is mounted in a rotary stage to easily allow both vertical and horizontal beam scans. Several different optical approaches were considered for producing reasonably quantifiable far- and near-field beam profile

measurements. The arrangement settled on to make these records is shown in Figure 17. The CCD array is an extremely sensitive device; for that reason, the 4th pass output had to be reflected off of two uncoated optical wedges, and at full pump energy, a neutral density filter having an optical density of 4.0 had to be inserted into the beam to prevent CCD array saturation. The amplifier output was then focused by a 1 meter focal length positive lens. The clear aperture of this lens is over 12 times the diameter of the incident beam, assuring a negligible spherical aberration contribution to distortion. The minimum beam waists in the horizontal and vertical formed behind this lens were located and characterized. A 500 mm focal length lens was then introduced and the beam diameters in its focal plane were measured. As described below, these two measurements constitute a set of data that can be unambiguously related to the degree of beam spread compared to an unperturbed, diffraction-limited Gaussian beam profile.

Standard propagation techniques can be utilized to show that a Gaussian beam, which has propagated through a lens, has a spot size of  $\lambda f / \pi w_0$  at the focal plane of that lens, where  $\lambda$  is the laser wavelength,  $f$  is the focal length of the lens, and  $w_0$  is the waist size ( $1/e^2$  intensity radius) of the original Gaussian beam. This result is independent of the distance between the positions of the lens and the Gaussian beam waist. Thus by carefully characterizing the waist size of the beam that is going into the 500 mm focal length lens, we can calculate what the spot size at its focal plane would be if the input were a perfect Gaussian. By taking the ratio of the spot size actually measured at the focal plane to this calculated value we obtain a "times diffraction limited" estimate for the actual beam. This estimate is reasonably accurate since the spatial profiles of all the beams we encountered were only slightly perturbed from the ideal Gaussian shape.

It should also be noted that the spatial beam profiles at the position of the minimum waists formed by the 1 m focal length

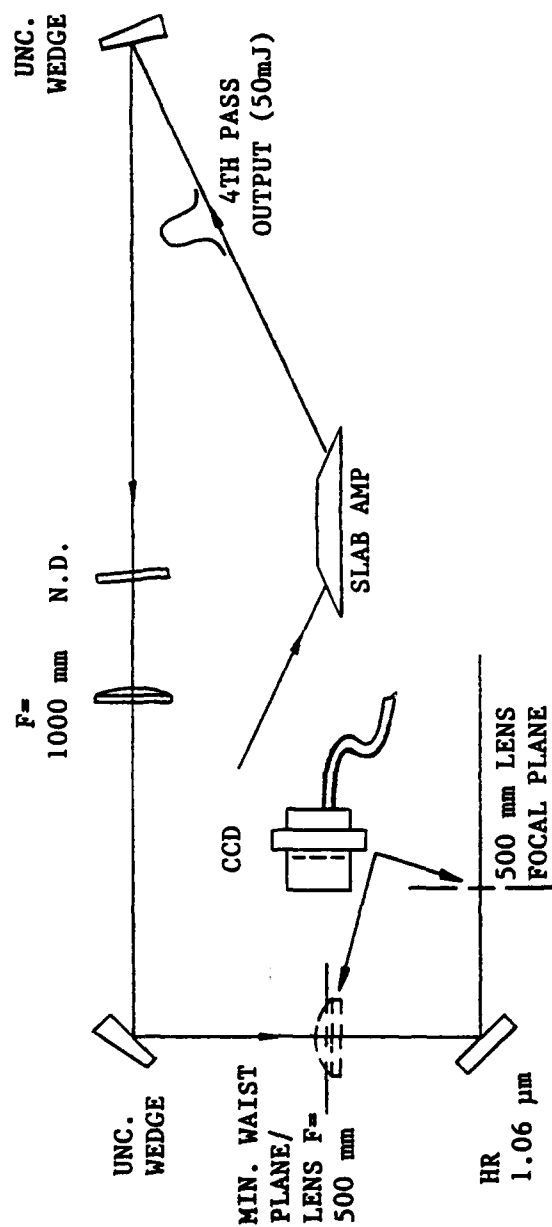


Figure 17. Experimental apparatus used in making horizontal and vertical CW and pulsed beam profile measurements.

lens are essentially equivalent in shape to the far field profiles. [The actual far field profiles would be obtained by looking at the spatial profiles at the focal plane (Fourier transform plane) of the 1 m lens, not at the minimum waist position which for these experiments we found to be  $\sim 1.15$  m behind the 1 m lens. We spot checked several times and always found that the spatial profiles 1 m behind the 1 m lens were essentially identical in shape to those at the minimum waist positions.] The profiles observed at the focal plane of the 500 mm lens reflect the near field profiles. [The profile at the focal plane of the 500 mm lens is the Fourier transform of the far field profile created at the focal plane of the 1 m lens. This double transform brings the profile back to the original near field pattern at the focal plane of the 500 mm lens.]

In the following we describe the measurements and provide photographs showing the spatial profiles of the beams in various operating regimes. Three main operating regimes were characterized: passive CW, high energy single-shot, and high energy, high pulse repetition frequency (PRF) operation.

#### Passive CW Operation

Many passive (no amplification, AOM set for continuous diffraction) CW profile measurements were made during the course of this work. Records of horizontal and vertical profiles were made in the vicinity of the amplifier input for system diagnosis and beam shaping purposes, as well as in the 4-pass performance setup shown in Figure 17. For these CW measurements the wedges (see Figure 17) were replaced by mirrors and the beam intensity on the CCD was controlled using ND filters. The passive data is of particular importance since it constitutes a "best-form" baseline beam quality against which to compare the actively pumped results.

A minimum beam diameter behind the 1 m lens was mapped out and found to be approximately coincident in the horizontal (H) and vertical (V) planes (i.e. passive beam astigmatism was found to be quite low). It should be emphasized that this minimum beam

diameter is not necessarily coincident with the 1000 mm back focal plane of the lens due to divergence or convergence that the 4th pass output beam may possess; and in fact, this smallest-beam plane was found to be located 1.15 m behind the 1.0 m lens. Beam diameters at the  $1/e^2$  points and spatial profiles were recorded (Figure 18, top row) for that plane. The 0.5 m focal length lens was then installed and the array was moved to that lens' focal plane. These H and V beam diameters and the spatial profiles are shown in Figure 18, bottom row. Using the technique discussed above, we obtain the following estimates of the beam quality:

$$\frac{2W_{500mm}(V) \text{ (meas'd)}}{2W_{500mm}(V) \text{ (calc'd)}} = \frac{0.95 \text{ mm}}{0.89 \text{ mm}} \Rightarrow 1.07 \times \text{diffraction limited}$$

$$\frac{2W_{500mm}(H) \text{ (meas'd)}}{2W_{500mm}(H) \text{ (calc'd)}} = \frac{0.71 \text{ mm}}{0.69 \text{ mm}} \Rightarrow 1.03 \times \text{diffraction limited}$$

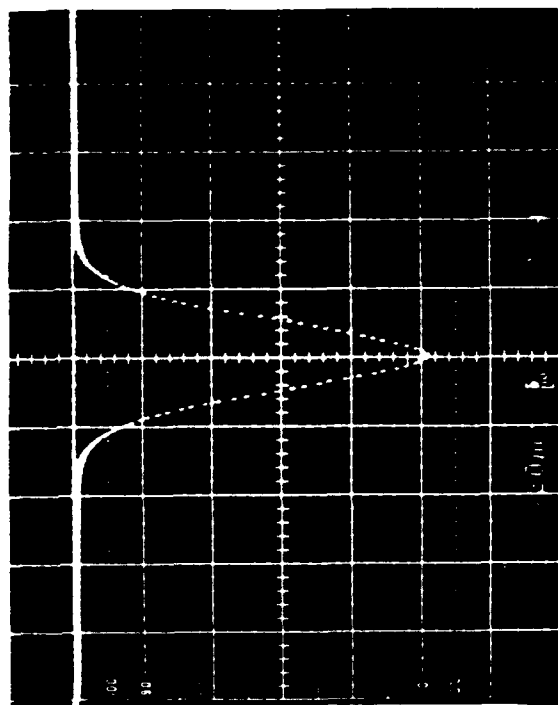
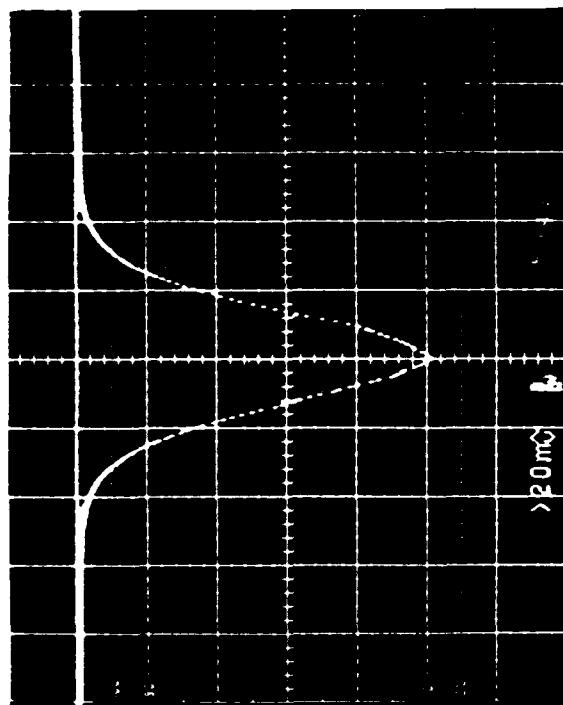
Thus, a baseline beam condition which is essentially diffraction limited has been established.

### Single-Shot Operation

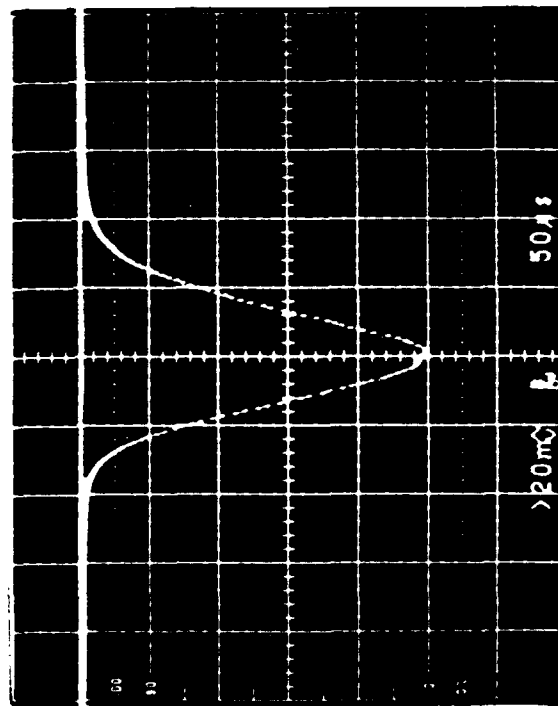
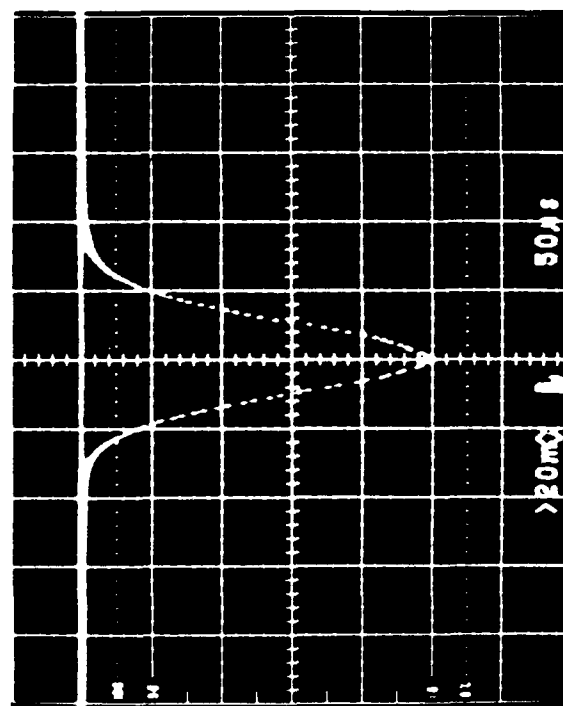
A useful intermediate result is obtained by operating the amplifier at full pulse energy (50 mJ 4-pass output in a 1  $\mu$ sec pulse) but at a repetition rate that is low enough that no new thermal equilibrium condition is reached compared to passive operation and the amplifier is effectively in a "single-shot" regime.

The same technique, as described above, was used to measure the minimum beam size behind the 1.0 m lens, which remained in the same plane as the passive work (i.e. no appreciable focusing is occurring in single-shot mode, as expected). Profiles in this plane were recorded (Figure 19, top row) and then the 500 mm lens was inserted into the beam in order to analyze the intensity profiles at its focal plane (Figure 19, bottom row). When these  $2w$  waist dimensions are treated in the same way as the passive-operation data, we find:

H



V

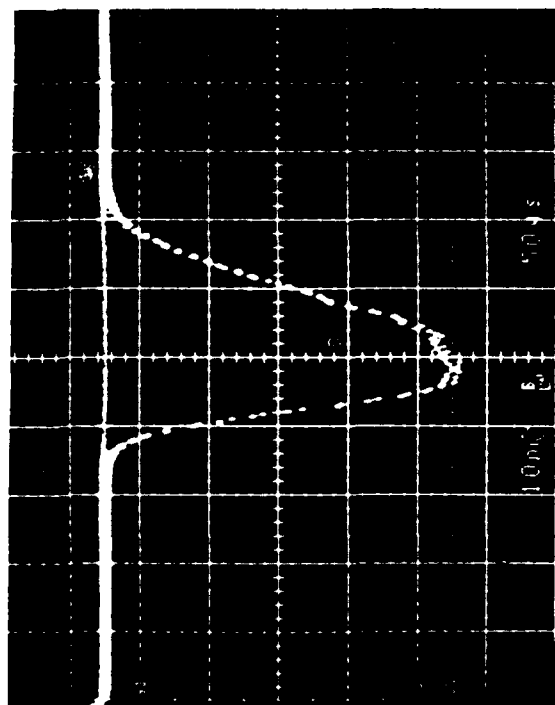
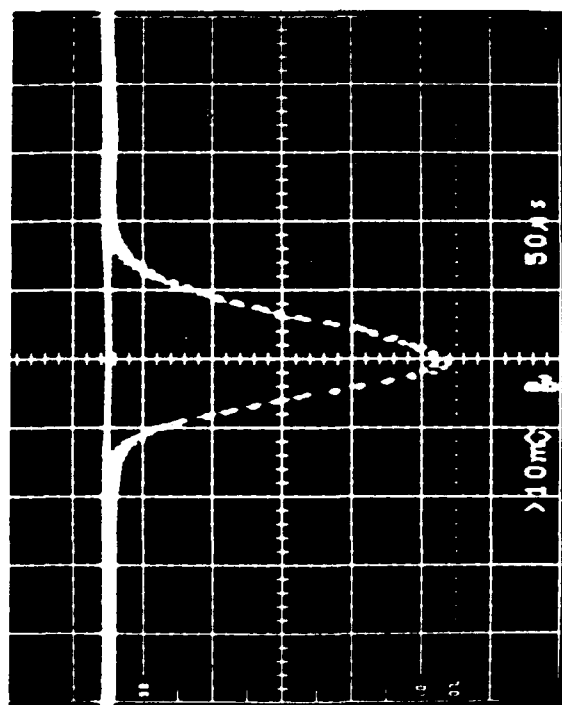


— DISTANCE (6.99  $\mu\text{m}/\mu\text{sec}$ ) —

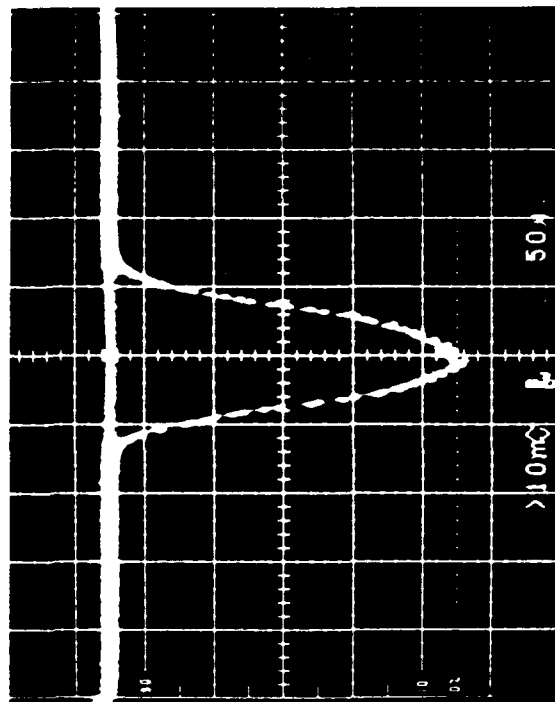
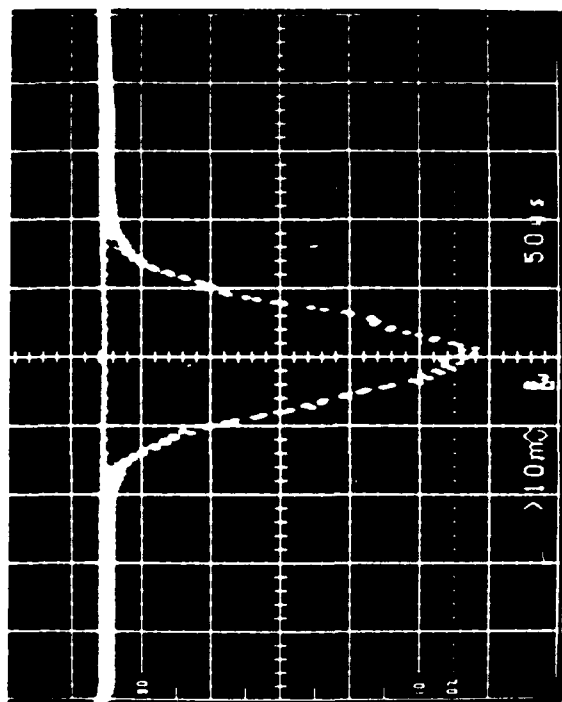
Figure 18. Passive, CW beam profiles. Top row: minimum beam diameters formed by 1m lens; V= 0.76mm, H= 0.98mm. Bottom row: back focal plane of 500mm lens; V= 0.95mm, H= 0.71mm.

INCREASING INTENSITY →

V



H



— DISTANCE ( $6.99 \mu m/\mu sec$ ) —

Figure 19. Full energy, single-shot pulsed beam profiles. Top row: minimum diameters formed by 1m lens,  $V=0.77mm$ ,  $H=0.90mm$ . Bottom row: back focal plane of 500mm lens,  $V=0.98mm$ ,  $H=0.74mm$ .

— INCREASING INTENSITY —

$$\frac{2W_{500\text{mm}}(V) \text{ (meas'd)}}{2W_{500\text{mm}}(V) \text{ (calc'd)}} = \frac{0.98 \text{ mm}}{0.89 \text{ mm}} \Rightarrow 1.11 \times \text{diffraction limited}$$

$$\frac{2W_{500\text{mm}}(H) \text{ (meas'd)}}{2W_{500\text{mm}}(H) \text{ (calc'd)}} = \frac{0.74 \text{ mm}}{0.75 \text{ mm}} \Rightarrow 0.99 \times \text{diffraction limited}$$

Of course the lower value is in slight error since a beam cannot be less than diffraction limited. The result is probably due to the fact that the spatial profiles are deviating from Gaussian as amplifier gain saturation takes place. Note the lower curves of Figure 19 which, as described earlier, essentially reflect the near field intensity patterns. In any event the reasonably close match to the passive-amplifier results indicates that no appreciable problems in amplifier operation appear to have developed at this point.

#### High Average Power Operation

The next step in characterizing the existing slab amplifier's beam quality involved operating at the highest average power currently possible, given the limitations of the flashlamp power supply. At present, the DC supply allows 12 Hz operation at 28-29 J, or about 340 W average power. We therefore undertook an effort to fully characterize the slab performance under these pumping conditions. The technique employed was identical to that described above for passive and single-shot beam profiling of the 4th-pass output.

Previously unknown problems with the existing multi-pass amplifier pump chamber hardware were discovered in the early stages of making these measurements which considerably complicated the process. It was found that under high average power loading (conditions the existing hardware was not explicitly designed for), the white delrin pump chamber end connectors absorb substantial amounts of heat from the xenon flashlamp, as do stainless steel flanges and connecting rods in close proximity to the lamp. The plastic end connectors are poor heat conductors and evidently become very non-uniformly heated.



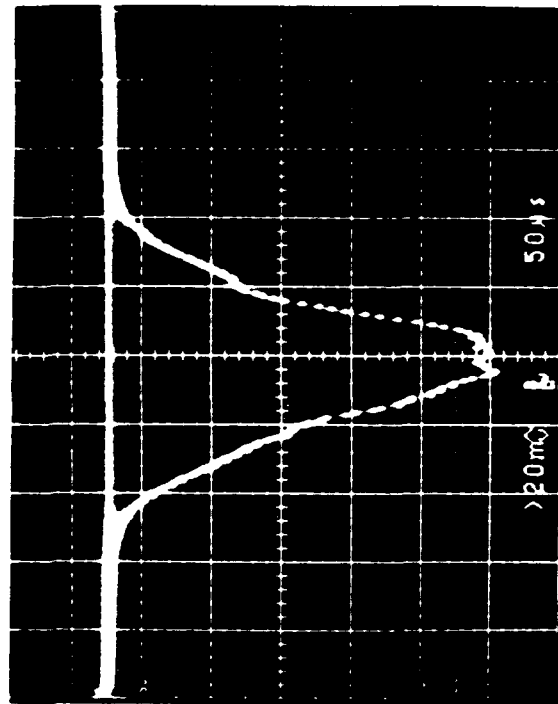
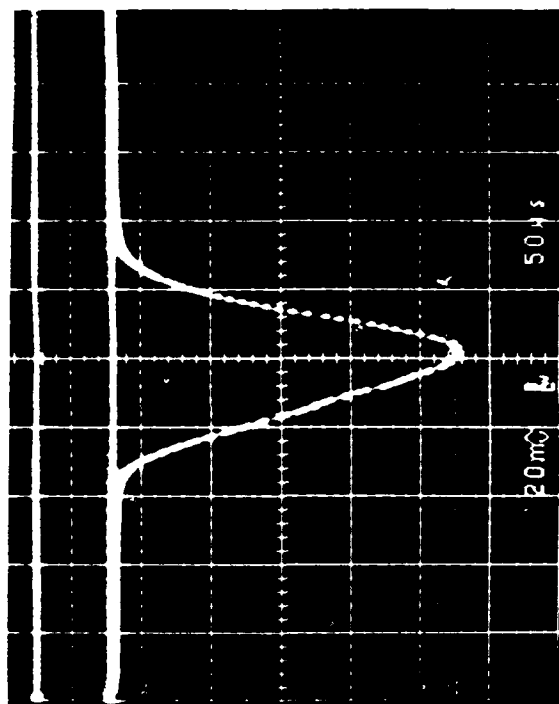
The delrin and stainless pieces, in turn, become very hot and have no conductive path to dissipate that heat. The combined effect of this non-uniform heating, over time, results in mechanical bending and expansion of the assembly which, in turn, produces severe vertical beam misalignment in the slab. The effect is accumulative; that is, the misalignment becomes more and more pronounced in the output of each successive amplifier pass, until the 4th pass input beam is almost entirely missing the 4 mm square aperture within ~ 10 minutes of continuous, high PRF operation, if not corrected. We are currently designing modifications to the amplifier hardware to remedy this heat removal problem. The only near-term solution to this problem was to determine the maximum permissible average power loading which still resulted in no misalignment, and restrict 12 Hz operation to that level. To completely avoid this problem we chose to run the amplifier at 12 Hz for only ~ 8 seconds every 3 minutes. The Nd:YAG slab alone is estimated to be at the new high repetition-rate-defined, steady state thermal condition within ~ 2 sec, so any beam distortion caused by the higher power loading in the slab was clearly evidenced by the end of an 8 sec operating interval.

With these restrictions in the amplifier operation at 12 Hz taken into account, it was eventually possible to map out the minimum beam waists as illustrated in Figure 17 and record the appropriate beam profiles. Again, minimum beam diameters in H and V were found to fall very close to the same plane found in the passive and single-shot cases. These profiles are shown in Figure 20, along with their respective profiles at the focal plane of the 500 mm lens. When the calculated spot sizes are compared to actual measurements at the focal plane, as described earlier, we find:

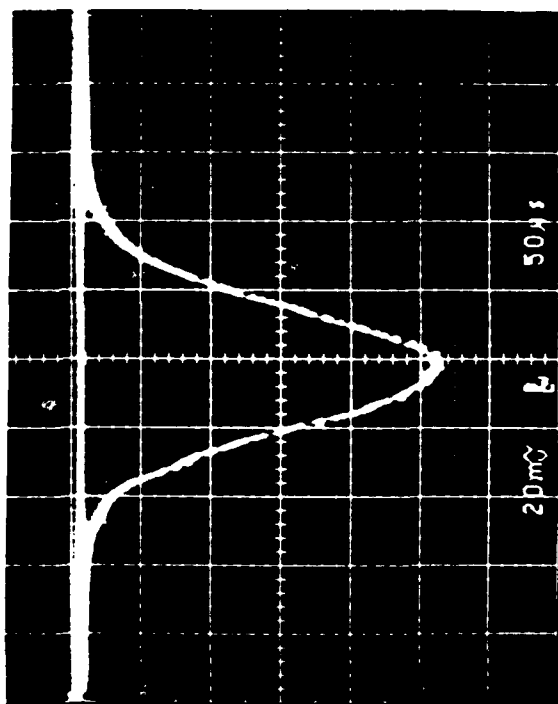
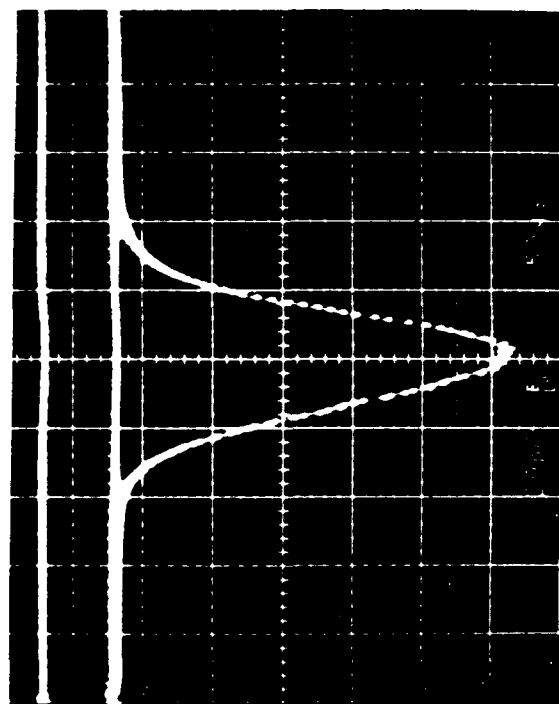
$$\frac{2W_{500mm}(V) \text{ (meas'd)}}{2W_{500mm}(V) \text{ (calc'd)}} = \frac{1.19 \text{ mm}}{0.75 \text{ mm}} \Rightarrow 1.59 \times \text{diffraction limited}$$

$$\frac{2W_{500mm}(H) \text{ (meas'd)}}{2W_{500mm}(H) \text{ (calc'd)}} = \frac{1.20 \text{ mm}}{0.78 \text{ mm}} \Rightarrow 1.53 \times \text{diffraction limited}$$

H



V



INCREASING INTENSITY →

— DISTANCE (6.99  $\mu\text{m}/\mu\text{sec}$ ) —

Figure 20. Full energy, 12 Hz pulsed beam profiles. Top row: minimum diameters formed by 1m lens,  $V=0.92\text{mm}$ ,  $H=0.87\text{mm}$ . Bottom row: back focal plane of 500mm lens,  $V=1.19\text{mm}$ ,  $H=1.20\text{mm}$ .

Thus, we see that 340 W power loading has an effect on the wavefront quality compared to passive operation. It should be noted that, as described in the beginning of Section 5, the single-wide slab used for these measurements had no edge insulation in place. This insulation would almost certainly improve the high PRF performance.<sup>2</sup> Due to time constraints of this effort, we could not repeat the wavefront distortion measurements using edge insulation, but we plan to do so in the near future. In any event the uninsulated 12 Hz performance remains reasonably near diffraction-limited. Higher resolution 2D profiling and active interferometry will be needed to better define distortion levels in future work.

## **6. Preliminary Design of a Diode-Pumped High Performance Slab Amplifier**

In order to meet the stringent beam quality, high average power, and efficiency requirements of remote target tracking and recognition applications, a specific course of action must be identified which will result in a diode laser array-pumped version of the multiple-pass slab amplifier described above. We believe that we have identified an approach which is economically and technically feasible for attaining that goal in the near term. The preliminary design of an all-solid-state multi-pass preamplifier capable of  $\sim 100$  Hz, high-gain operation is described below.

### **6.1 Pump Source Considerations**

The basic geometry of the miniature Brewster-ended zig-zag slab lends itself quite effectively to transverse, 2-D laser diode array pumping schemes. The zig-zag slab is inherently capable of operation at high average powers, and the use of diode pumping roughly triples its power handling capacity.<sup>10</sup>

Two-dimensional diode array technologies currently available and demonstrated can be separated into 3 categories:

- Stack-and-Rack Bar Arrays
- Fiber-Coupled Bars
- Monolithic 2D Arrays

Stack and rack arrays are the most technologically mature and economical devices available at this time that are appropriate for providing the pump powers necessary in this amplifier. These are typically  $1\text{ }\mu\text{m} \times 1\text{ cm}$  diode laser bars, mechanically stacked to produce two dimensional arrays of  $(n)\text{ cm} \times 1\text{ cm}$  dimensions. These arrays can then in turn be arranged side-by-side to produce long, narrow diode array assemblies suitable for slab amplifier transverse pumping. Quasi-CW operation of these arrays is commonly used to produce high-peak power pump pulses of  $\sim 200\text{ }\mu\text{s}$  duration. Numerous near-term technological and manufacturing hurdles still exist for fiber-coupled, quasi-CW bars and for truly monolithic, high-power 2-D arrays. For this reason, we have concentrated our design on commercially proven and available pulsed stack-and-rack arrays. Spectra Diode Labs, Inc. (SDL) has pursued this technology most aggressively and is rapidly realizing significant performance gains and cost reductions in the arrays of interest in this design. Our preliminary specification and cost analysis is based on the most current diode array information provided to us by SDL workers.

## 6.2 Preliminary Design of Diode-Pumped Amplifier

### Amplifier Pump Analysis

In the following we consider diode pumping a slab whose dimensions are approximately the same as those given in Table 1. The goal is to estimate the diode laser pump energy/pulse required to maintain the level of performance described in Section 5 for the flashlamp pumped slab.

First, assume that the diode laser light is collimated so that it pumps only the central 2.5 mm section of the 4.0 mm wide slab. This allows better overlap between the laser mode volume and the pumped volume, while avoiding hard aperture effects and

minimizing wavefront distortion (see Section 4). The energy storage required to produce a small-signal gain of  $G_0$  can be calculated using

$$E_{\text{stored}} \sim h\nu N_{\text{total}} = \frac{h\nu A_p}{\sigma} \left[ \frac{L_p}{L} \right] \ln G_0 \quad (33)$$

where, for the case at hand,  $A_p \sim 0.095 \text{ cm}^2$  ( $0.25 \times 0.38 \text{ cm}$ ) is the cross sectional area of the pumped volume,  $\sigma \sim 3.5 \times 10^{-19} \text{ cm}^2$  is the stimulated emission cross section for Nd:YAG,  $h$  is Planck's constant,  $\nu$  is the laser frequency,  $G_0$  is the desired small signal gain, and  $L_p/L$  is the ratio of the length of the pumped volume to the length of the beam path in the pumped volume. For example, a 21-bounce zig-zag path (3rd pass in Figure 9) through the slab described in Table 1 gives  $L_p/L \sim 0.77$ . (It should be noted that Eq. (33) is a simple variation of Eq. (5) of Section 3.)

Using the above parameters in Eq. (33) we find that a stored energy of  $\sim 200 \text{ mJ}$  is required if a single-pass small-signal gain of 22 dB is desired. The diode pump energy,  $E_p$  required to create this amount of stored energy is obtained using

$$E_{\text{stored}} = \eta_q \eta_{ab} \eta_{fl} E_p \quad (34)$$

where  $\eta_q = \lambda_p/\lambda_l$  is the ratio of the pump wavelength to the laser wavelength (i.e., the quantum defect),  $\eta_{ab}$  is the fraction of the pump energy  $E_p$  that actually gets absorbed in the mode volume, and  $\eta_{fl}$  represents the reduction in stored energy due to decay of the inversion during the pump pulse. The value of  $\eta_{fl}$  is given by

$$\eta_{fl} = \frac{\tau_2}{\tau_p} \left[ 1 - \exp(-\tau_p/\tau_2) \right], \quad (35)$$

where  $\tau_2$  is the 230  $\mu\text{s}$  lifetime of the upper laser level in Nd:YAG and  $\tau_p$  is the duration of the pump pulse.

For a 200  $\mu$ s pump pulse duration, Eq. (35) gives  $\eta_{fl}=0.67$ . A reasonable estimate for  $\eta_{ab}$  is 0.85 since the absorption coefficient of 1% doped Nd:YAG is  $\sim 5 \text{ cm}^{-1}$ . Using  $\eta_q = 0.76$ ,  $\eta_{fl} = 0.67$ ,  $\eta_{ab} = 0.85$ , and  $E_{\text{stored}} = 200 \text{ mJ}$  in Eq. (34) give  $E_p = 460 \text{ mJ}$ . As described below, this level of pump energy can be achieved by using  $\sim 8$  commercially available quasi-cw diode laser arrays.

If four passes are made through a well-designed high-gain slab amplifier like the one described here, input pulse energies of only 10-100 nJ can lead to 30% or greater extraction of the stored energy (see Sections 3 and 5). For this example, 30% extraction implies pulse energies of  $\sim 60 \text{ mJ}$ . When this is compared to the energy of the pump pulse ( $E_p \sim 460 \text{ mJ}$ ) we see that the optical to optical conversion efficiency of this device can be  $> 13\%$ . Since the electrical to optical efficiency of diode lasers is typically  $\sim 35\%$ , the electrical to optical efficiency of the slab preamplifier can be  $> 4.5\%$ . Although this does not include power for cooling it is still impressive for a preamplifier which takes nJ input pulses and amplifies them to many mJ.

### Amplifier Geometry

Given the physical and technological constraints detailed above, we have arrived at a very preliminary design of an all-solid-state multiple-pass Nd:YAG amplifier, feasible for construction in an SBIR Phase II effort. It is stressed that this design is still only highly conceptual, and a major task in any effort to successfully realize such an amplifier will involve conducting analyses of several critical issues, among them optimum pump light collection and delivery, slab and diode array cooling, and slab geometry optimization for specific pump source and average power loading requirements. Nevertheless, as a result of our previous experience and the conclusions detailed in Sections 4 and 5, enough of the fundamental design problem is understood at this point to direct initial component specifications and cost estimates.

Figure 21 illustrates the conceptual design of an amplifier using a miniature zig-zag slab of similar dimensions to the slab used in the experiments conducted during this contract. The size of this slab lends itself very well to pumping by a series of eight SDL quasi-CW, 5-bar array stacks. Each bar emits 60 W peak at 808 nm wavelength, for a total 8-module pump power of 480 mJ/pulse, or 2.4 kW peak power in 200  $\mu$ sec pulses. As outlined above, this pump level is sufficient to achieve the energy storage necessary for efficient operation. These arrays are currently rated for a duty cycle of 1.5% or 75 Hz operation. SDL assures us that there is no problem with 100 Hz operation.

The eight individual stack-and-rack array modules have effective emitter dimensions of 1.6 mm x 10 mm. The output is essentially diffraction-limited in the narrow dimension and highly incoherent in the long dimension. The diffraction-limited direction is highly divergent due to the narrow emitting aperture of  $\sim 1 \mu$ m, and cylindrical optics must be carefully designed and incorporated between the series of arrays and the slab for efficient transverse pumping of the central 2.5 mm region of the 4 mm-high piece. By selectively pumping only the volume filled by the input signal, the amplifier extraction efficiency is improved compared to flashlamp pumping, and pump power requirements can be somewhat relaxed. Since the absorption coefficient of 1% doped Nd:YAG is  $\sim 5 \text{ cm}^{-1}$ , about 13% of the pump energy is transmitted through the 4 mm thick slab. It may be possible to reflect this transmitted light back through the slab by using a high reflector for 810 nm radiation, bringing the pump absorption to nearly 100%. A normal incidence mirror, as shown in Figure 21, may adversely effect the diode laser output, due to feedback. If this causes difficulty the mirror could be tilted slightly or even removed. Operating without the mirror will only cause a small decrease in the overall efficiency of the amplifier, since only  $\sim 13\%$  of the pump light is lost. Although we do not anticipate the need (see discussion above) even more pump energy could be supplied by replacing the mirror in Figure 21 with additional diode bars.

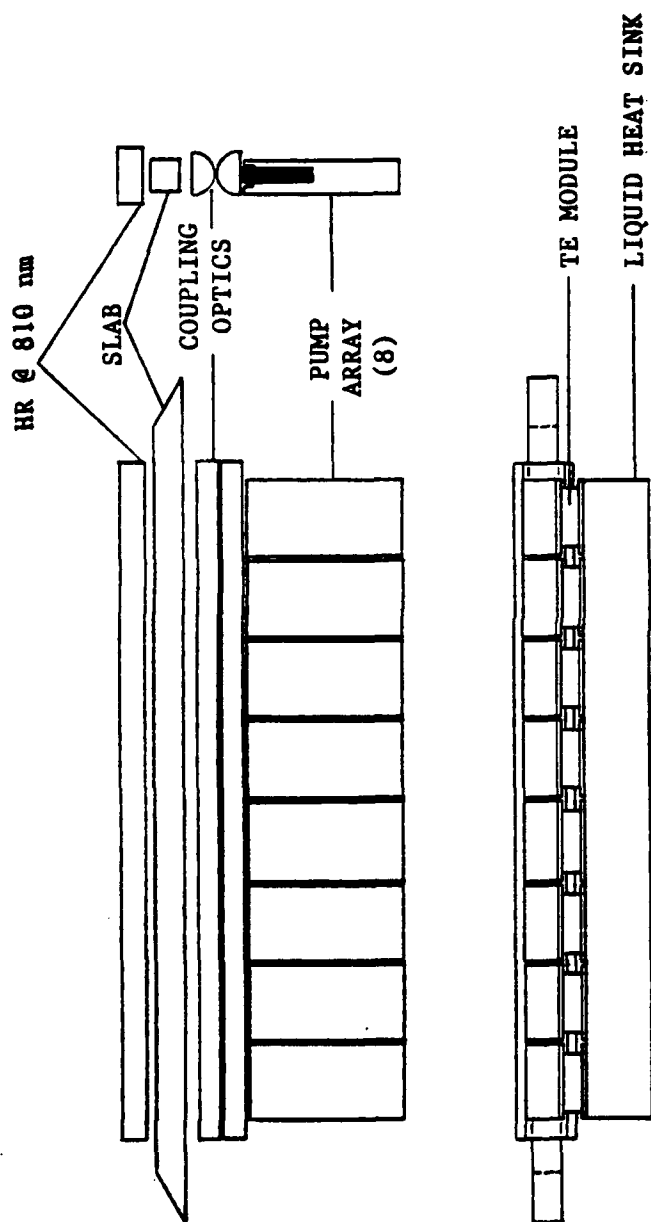


Figure 21. Conceptual design of a laser diode array-pumped multiple-pass Nd:YAG slab amplifier.



Amplifier slab cooling is an area of the design which is left open at this stage. The quantum defect of the 810 nm pump photons compared to 1.06  $\mu\text{m}$  output implies that the heat load in the Nd:YAG slab is only  $\sim 25\%$  of the diode arrays output, or about 10 W in this conceptual design. This load could well be dissipated passively, or through relatively simple and efficient conductive and/or forced convective means. Control of internal parasitic paths so that high gain can be achieved also figures into the choice of slab cooling, as a high-index medium (such as water, in our current flash-pumped amplifier) may be essential to increase the critical angle for total internal reflection and thus inhibit many parasitic modes supported in the slab in air. Thick-film technologies should be investigated as a means of providing this high-index interface, as well.

SDL and other laboratories continue to improve the wafer growth techniques that ultimately determine the wavelength spread and variation in emitter junction temperature of individual array elements. Nevertheless, present day practical limits on matching the operating currents and electrical efficiencies, and hence the peak output wavelengths of multiple-bar array stacks lead us to conclude that each stack must be individually controlled in temperature (Figure 21, side view). These devices must be temperature-tuned at a rate of about  $0.3 \text{ nm}/^\circ\text{C}$  in order to uniformly pump at Nd:YAG's absorption peak at 808-810 nm. A relatively inefficient but technically mature means of achieving this wavelength matching condition is with the use of thermo-electric (TE) cooler modules. A liquid-cooled heat exchanger is then used to remove the excess heat from the TE modules. Silicon micro-channel substrate coolers, or CHIC coolers, are rapidly undergoing development at Lawrence Livermore National Laboratory, MIT Lincoln Laboratory, and other laboratories. This technology holds much promise for highly efficient diode array pump heat removal and wavelength control, and should be assessed for use in this amplifier as well.

The technology now exists to construct a highly efficient multi-pass preamplifier of the type suggested above. A compact,

immediately useful device would result which would also form the knowledge base from which even more efficient, powerful, and cost-effective designs would result.

### Cost Estimate

We have investigated the cost of components of an amplifier having basically the form sketched in Figure 21, as an example of how such a development effort has become eminently feasible in recent months. Such an estimate is almost inherently pessimistic with time, given the continuously dropping cost and increasing performance of the laser diode pump arrays.

#### Diode-Pumped Nd:YAG Multi-Pass Amplifier Estimated Cost

	\$ x 1000
1. Diode pump arrays (SDL 3230-TD), properly selected for wavelength and current operation -	216
2. Current driver/control system for pumps -	50
3. Thermo-electric wavelength control system -	25
4. Liquid-cooled array heat sink system -	5
5. Multi-pass Nd:YAG slab -	20
6. Amplifier head/slab cooling system design and development -	<u>150</u>
TOTAL	466

### 7.0 Summary and Conclusions

The promise of an agile all-solid state 1.06- $\mu$ m coherent laser radar led us to investigate the development of an efficient diode laser-pumped Nd:YAG preamplifier. A very high gain preamplifier is needed; one which is capable of taking low energy (10-100 nJ) long-duration input pulses and amplifying them to the 10's of mJ necessary for saturation and efficient energy extraction in the following stages of amplification. The preamplifier we investigated utilizes a slab geometry which permits several angularly-multiplexed passes through the gain

medium to be made, allowing the stored energy and hardware to be efficiently used.

A key difficulty of the multiple-pass slab design is the necessity of demanding flatness of the reflecting surfaces. The large number of bounces from the slab faces can lead to high accumulated wavefront distortion. In this report we show that high quality slabs of the proper dimensions for this application can be fabricated and that low distortion amplification can be achieved.

An existing flashlamp-pumped Nd:YAG slab was utilized during this effort to demonstrate that efficient preamplification of low energy pulses can be achieved. Using this less-than-ideal slab in a 4-pass amplifier configuration we demonstrated: 1) small signal gains exceeding 87 dB ( $>5 \times 10^8$ ); 2) output pulse energies exceeding 50 mJ, for input pulse energies  $< 50$  nJ; and 3) spatial beam quality  $< 1.5$  times diffraction limited, even at moderately high average pump power.

We also performed the preliminary design of a diode laser-pumped version of this slab preamplifier. Our analysis shows that this diode pumped preamplifier should be capable of overall electrical to optical efficiencies of 3-5%. This is very good for a single preamplifier which takes very low energy (10-100 nJ) long-duration input pulses and amplifies them to 50 mJ and higher. We also show that the development of the diode pumped preamplifier fits well within the cost constraints of a Phase II SBIR program. We recommend that work proceed in developing the highly-efficient, diode laser-pumped, high-gain preamplifier.

## 8. References

1. G.J. Hulme and W.B. Jones, "Total Internal Reflection Face Pumped Laser," Proc. Soc. Photo-Opt. Instrum. Eng. 69, 38 (1975).
2. T.J. Kane, R.C. Eckhardt, and R.L. Byer, "Reduced Thermal Focusing and Birefringence in Zig-Zag Slab Geometry Crystalline Lasers," IEEE J. Quantum Electron. QE-19, 1351 (1983).
3. T.J. Kane, J.M. Eggleston, and R.L. Byer, "The Slab Geometry Laser - Part II: Thermal Effects in a Finite Slab," IEEE J. Quantum Electron. QE-21, 1195 (1985).
4. T.J. Kane, W.J. Kozlovsky, and R.L. Byer, "62-dB-gain multiple-pass slab geometry Nd:YAG Amplifier," Opt. Lett. 11, 216 (1986).
5. M.J. Kavaya, S.W. Henderson, and R.M. Huffaker, "Development of a Pulsed 1.06-Micron Solid State Coherent Laser Radar for Wind Velocity and Aerosol Backscatter Measurements" (November 1988). CTI Technical Report 8806, Final Report for AF Contract F04701-86-C-0085.
6. M.J. Kavaya, S.W. Henderson, J.R. Magee, C.P. Hale, and R.M. Huffaker, "Remote wind profiling with a solid-state Nd:YAG coherent lidar system," Opt. Lett. 14, 776 (1989).
7. J.M. Eggleston, L.M. Frantz, and H. Injeyan, "Derivation of the Frantz-Nodvik Equation for Zig-Zag Optical Path, Slab Geometry Laser Amplifiers," IEEE J. Quantum Electron. QE-25, 8 (1989).
8. A.E. Siegman, Lasers, University Science Books, Mill Valley, CA (1986).
9. T.J. Kane, "Coherent Laser Radar at 1.06 Microns Using Solid State Lasers," PhD. Thesis, Stanford University (1986).
10. T.S. Chen, V.L. Anderson and O. Kahan, "Measurements of Heating and Energy Storage in Diode-Pumped Nd:YAG," IEEE J. Quantum Electron. QE-26, 6 (1990).